SAND99-1567J

ISSUES ARISING FROM PLASMA-WALL INTERACTIONS IN ITER-CLASS TOKAMAKS

3. Review of physical processes and underlying theory

3.4 H interactions with wall materials

3.4.1

This section reviews physical processes involved in the implantation of energetic hydrogen into plasma facing materials and its subsequent diffusion, release, or immobilization by trapping or precipitation within the material. These topics have also been discussed in previous reviews [1,2,3]. The term "hydrogen or H" is used here generically to refer to protium, deuterium or tritium.

Implantation

Implantation of energetic particles into solids is fairly well understood [4]. In tokamaks, plasma-facing materials are bombarded by energetic ions and neutrals from the plasma with energies up to a few keV. As these energetic particles penetrate into a solid they lose their kinetic energy, mainly to electrons, and are deflected by collisions with atoms thereby transferring kinetic energy to atoms in the solid. Some of the incident particles scatter back out of the material with a significant fraction of their initial energy. The fraction of particles which backscatter is higher for lower incident energies and higher Z target materials and can exceed 50% [5]. Particles which do not backscatter eventually come to thermal energies within the material and settle into an atomic configuration which has a local energy minimum. The depth distribution of these implanted particles depends on the energy and atomic number of the incident particles and on the target material.

Atomic collisions displace atoms from their equilibrium lattice sites. If the transferred energy is less than a few tens of eV a metal lattice will relax back to its original atomic configuration. Collisions transferring more energy than this can produce lattice vacancies and interstitials. The maximum energy transferred in a collision is

$$E_t = E_o \, 4M_1M_2/(M_1+M_2)^2, \qquad (1)$$

DISCLAIMER

where E_o is the incident particle energy and M_1 and M_2 are the incident and target atom masses. Light projectiles therefore transfer a larger fraction of their energy to light target atoms than to heavy target atoms. Thus in a plasma wall environment, such displacement defects are more likely to be produced in low Z materials than in high Z materials. In metals a vacancy/interstitial pair is dynamically unstable and will recombine if their separation is less than a few lattice spacings. This limits the concentration of displacement defects to less than about 1 atomic percent, even in the absence of long range mobility. Vacancies and interstitials also migrate by thermally activated diffusion and disappear at surfaces and dislocations, annihilate by recombining with each other or agglomerate into less mobile defect clusters. Defect mobility depends on the material and on temperature. Interstitial atoms are mobile above about 100 K in most metals. Vacancies become mobile at an absolute temperature which is roughly a quarter of the melting temperature. Vacancies may also capture hydrogen, as will be discussed later in this section, which may reduce their mobility. The extent to which atomic displacements by energetic hydrogen influence plasma wall interactions is not well understood, but these defects are more likely to have a significant effect for low Z materials than for high Z materials. Monte Carlo computer simulations of implantation have been developed which are widely used to calculate depth profiles of implanted atoms and displaced lattice atoms, and the energy and angular distributions of backscattered particles [6,7].

Hydrogenic ions from a plasma typically have energies in the range from tens to hundreds of eV after acceleration through a sheath potential. The energy distribution of charge exchange neutrals depends on the density and ion temperature profile in the plasma edge and can extend up to a few keV for hot low-density plasmas. In low Z materials such as C or Be, the depth of implantation of hydrogen with energies of 0.1 to 1 kev is about 3 to 30 nm [8]. At a given energy, the depth of implantation of hydrogen into high Z materials is less than in low Z materials.

Diffusion in metals

Hydrogen implanted into metals will predominantly come to rest at interstitial solution sites. From there the hydrogen may hop to neighboring solution sites thus undergoing thermally activated diffusion. The fate of implanted hydrogen strongly depends on its mobility through the lattice, hence on the temperature. In most metals

hydrogen diffuses at room temperature and above [9]. In this case the time dependent distribution of hydrogen in the material can be described by the diffusion equation:

$$\frac{\partial C_s(x,t)}{\partial t} = D\frac{\partial^2 C_s}{\partial x^2} + \Phi\, P(x) - \sum_i S_i\,, \qquad (2)$$

where $C_s(x,t)$ is the concentration of hydrogen in solution per host atom and D is the diffusion coefficient for hydrogen in solution. The second term is the source term for implanted hydrogen where Φ is the flux and P(x) is the depth distribution. Source/sink terms S_i describe other processes which add to or subtract from the concentration of hydrogen in solution. Such processes include trapping and internal precipitation into gas phase or hydride phase. In addition, a boundary condition at the surface is required. Release of hydrogen from a metal surface normally occurs by the desorption of hydrogen molecules. The direct thermal desorption of atomic hydrogen from the surface occurs at a much slower rate due to the larger energy barrier for this process. For release by molecular recombination at the surface the outgoing flux (atoms per unit area and time) is

$$\Phi_o = -D\,[\partial C_s/\partial x]_{x\to 0} = 2\,K_r\,[N\,C_s(x\to 0)]^2\,, \qquad (3)$$

where $C_s(x\to 0)$ and $[\partial C_s/\partial x]_{x\to 0}$ indicate the value and the gradient, respectively of the concentration of hydrogen in solution just beneath the surface, N is the atomic density of the host and K_r is a rate coefficient for molecular recombination. K_r can be determined in experiments which simultaneously measure hydrogen concentration and release rate [10], and theoretical models exist which give K_r values from first principles for bare metal surfaces[10-12]. Monolayer coverage of surfaces by contaminants such as oxygen, can reduce K_r by orders of magnitude [13]. Dissociative absorption of hydrogen from gas phase into solution in metals is similarly hindered by surface impurities[13]. This sensitivity of hydrogen uptake and release to surface contaminants often strongly affects permeation and thermal desorption experiments.

Trapping in metals

Trapping of hydrogen at lattice defects can strongly affect the behavior of hydrogen in materials. Here we define traps as non-interacting sites where hydrogen is atomically bound and where its energy is below that of a solution site. Examples of such sites are lattice vacancies, adsorption onto internal (i.e. void) surfaces and interfaces with embedded particles such as oxides. Figure 1 illustrates the relative energies of hydrogen

in various states in a metal host and the barriers for thermally activated transitions between states.

The condition for thermodynamic equilibrium between hydrogen in traps and hydrogen in solution is obtained by equating the chemical potentials of hydrogen in these two states. For static traps in which one hydrogen atom can be accommodated in each trap, statistical mechanics gives the equilibrium condition

$$C_s/z = C_t/(C_T - C_t) \exp(-Q_t/kT), \qquad (4)$$

between the concentration of hydrogen in solution C_s and the concentration of hydrogen in traps $C_t(x,t)$, where $C_T(x)$ is the concentration of traps, Q_t is the difference in enthalpy between hydrogen in a trap and at a solution site, k is Boltzmann's constant, T is temperature and z is the number of solution sites per host lattice atom. This expression assumes that the fraction of solution sites occupied by hydrogen is small and that the nonconfigurational or vibrational part of the entropy difference between trapped and untrapped hydrogen is small. The source/sink term describing the effect of static traps on hydrogen transport can then be formulated as

$$S_t = \partial C_t/\partial t = \Gamma[C_s(C_T(x) - C_t) - z\, C_t \exp(-Q_t/kT)], \qquad (5)$$

where Γ is the rate at which local equilibrium between hydrogen in traps and solution is approached. The left and right terms are the trapping and detrapping rates respectively. In equilibrium these terms are equal and $\partial C_t/\partial t = 0$. The rate coefficient can be expressed as

$$\Gamma = 4\pi NDR, \qquad (6)$$

where R the reaction radius, i.e. hydrogen–trap separation at which reaction occurs, which is about one lattice constant. Solutions to the transport equation usually depend only weakly on the value of the equilibration rate Γ. More critical is the condition for thermodynamic equilibrium (eq. 4). This is because features of interest usually involve longer range transport occurring over time scales long compared to the time to reach local thermodynamic equilibrium.

The case where a material contains more than one type of static trap can be described by including additional source/sink terms like equation 5, each with its own trap concentration and binding enthalpy. Appropriate source terms have also been included for situations where each trap may accommodate multiple hydrogen atoms, for example adsorption sites on the surface of internal cavities or multiple hydrogen atoms in a

vacancy [3]. This formalism has also been extended to include the case where multiple types of traps are themselves diffusing and interacting with each other to describe hydrogen interacting with displacement defects in nickel [14].

Trapping of hydrogen at vacancies and on surfaces of internal cavities has been extensively studied in many metals, both theoretically and experimentally by several methods. Experimental methods include studies of internal redistribution of deuterium between traps at different depths, equilibration of trapped deuterium with the known chemical potential of gas phase deuterium, thermal desorption, positron annihilation and perturbed angular correlation gamma emission. Much of this work for metals is reviewed in reference 3. A critical parameter for describing hydrogen trapping is the binding enthalpy of hydrogen to the traps. Table 1 gives values of binding enthalpy of D to vacancies at low occupancy in several metals obtained both from experiments and from first principles calculations.

Trapping of hydrogen at helium bubbles produced by implantation of helium into metals has also been studied extensively. This is relevant to fusion plasma environments where helium bubbles may be formed by implantation of fusion alpha particles, by tritium decay or by neutron induced transmutation. These studies show that helium bubbles in metals trap hydrogen even more strongly than vacancies. Table 2 summarizes binding enthalpies of D to helium bubbles in several metals obtained from experiments and theory. Trapping of hydrogen at helium bubbles is essentially the same mechanism as chemisorption onto a surface as can be seen from the fact that binding enthalpy of hydrogen to helium bubbles is similar to measured enthalpy of chemisorption onto external surfaces relative to hydrogen in a solution site. The high density helium in the small cavities does not significantly influence hydrogen trapping on the cavity surfaces.

As shown by tables 1 and 2 the binding enthalpies of hydrogen to vacancies and helium bubbles calculated by the effective medium theory are generally in good agreement with experimental values. The central concept behind the effective medium theory is an embedding function which gives the energy to insert an initially isolated atom, for example hydrogen or helium, at a particular site in terms of the unperturbed local electron density at that site before inserting the atom [18,19]. This function depends on the type of embedded atom but is independent of the host The approximate energy

obtained from the embedding function is then refined by incorporating host specific perturbation terms. Figure 2 shows the embedding functions for hydrogen and helium. A significant feature for hydrogen is the energy minimum at finite electron density which reflects its chemical reactivity, whereas the embedding function for helium, which is chemically inert, has no such minimum. For most metals the local electron density at the interstitial hydrogen solution site lies well above the minimum, hence any local dilation of the lattice will produce a trap for hydrogen by lowering the local electron density. Furthermore, the more open the defect the greater the binding enthalpy, with large voids and external surfaces providing the asymptotic limit. For example, monovacancies trap hydrogen substantially more strongly than dislocation strain fields or stacking faults, but somewhat less strongly than voids [3]. Trapping of hydrogen at substitutional impurities in metals is observed to be weak ($Q_t \leq 0.1$ eV typically) [20] as expected, since these do not create open volume. Metals with large endothermic heats of solution (i.e. low solubility), should have large values of Q_t for trapping at vacancies and surfaces, since the enthalpy difference between solution and trap sites will be larger as illustrated in figure 1. For example, molybdenum and tungsten have large endothermic heats of solution (0.68 and 1.04 eV respectively [21,22]) and large binding enthalpies (1.03 and 1.1 eV respectively [23,15,16]) for hydrogen trapped at vacancies. The combination of low solubility and strong trapping means that small defect concentrations can strongly influence hydrogen content and mobility which makes measurements of hydrogen solubility and diffusivity susceptible to errors due to trapping.

Because of its high atomic density, beryllium has one of the highest interstitial electron densities of any metal [24], and thus might be expected to represent an extreme case of low solubility and strong trapping for hydrogen. Experiments to measure hydrogen solubility in Be have found low concentrations of hydrogen in solution but often also small endothermic heats of solution [25]. This combination suggests that these solubility studies might be measuring occupation of hydrogen sites other than bulk solution in Be metal. The process normally used to fabricate beryllium, in which beryllium powder is vacuum hot pressed, leaves many small beryllium oxide inclusions, typically at volume fractions of 1%, which could provide trap sites at the metal/oxide

interface or lower energy solution sites within the BeO particles. Hydrogen is observed to be strongly trapped by such oxide inclusions in aluminum [26].

Precipitation.

If hydrogen in solution encounters an internal void it will precipitate as molecular hydrogen. If the void volume is connected to an external surface the gas will escape the material. Otherwise the gas pressure in the void will increase as hydrogen flows into it. Net flow ceases when thermodynamic equilibrium between solution and gas phases is reached, i.e when the chemical potentials of the two phases are equal. This gives

$$C_s/C(P_o) = (P^*/P_o)^{1/2}\,, \qquad (7)$$

when the fraction of solution sites occupied by hydrogen is small, where C_s is the concentration in solution. P^* is the fugacity of the gas, which for an ideal gas equals the gas pressure. The solubility

$$C(P_o) = C_{so}\exp(-Q_s/kT)\,, \qquad (8)$$

is the concentration of hydrogen in solution in equilibrium with gas at some reference pressure P_o small enough for the gas to behave ideally, Q_s is the enthalpy of solution and C_{so} is a solubility prefactor. Implantation of hydrogen into materials may produce concentrations of hydrogen in solution, for which the equilibrium gas pressure is very high. The fugacity and chemical potential μ can be obtained from the equation of state [27] relating the gas pressure P to the molar volume V_m by integrating

$$\ln(P^*/P_o) = (\mu-\mu_o)/kT = (kT)^{-1}\int_{Po}^{P} V_m(P')dP'\,. \qquad (9)$$

Precipitation of hydrogen into static cavities can be included in the transport equation through a source/sink term of the form

$$S_g = \partial C_g/\partial t = \Gamma_g[C_s - C_{eq}(C_g,V_c,T)], \qquad (10)$$

where $C_{eq} = (P^*/P_o)^{1/2}\,C_{so}\exp(-Q_s/kT)$

is the concentration of hydrogen in solution in equilibrium with the gas in the cavities, which depends on temperature and molar volume of gas in the cavities, and therefore on C_g , the quantity of hydrogen in the cavities and on V_c , the volume of cavities per unit volume of material since $C_g=2V_c/V_m$. (11)

The rate coefficient $\Gamma_g = 4\pi NDR_cN_c$, (12)

where R_c is the cavity radius and N_c is the number of cavities per unit volume.

The flow of hydrogen into cavities may lead to gas pressures high enough to cause the cavity volume to increase. The two principle mechanisms for growth of small cavities are absorption of vacancies and production of dislocations. Growth by emission of single interstitial atoms is energetically unfavored, compared to the collective process of dislocation production, except possibly for very small cavities approaching atomic dimensions. Absorption of vacancies produced by atomic collisions during implantation can contribute to cavity growth, although absorption of interstitial atoms which are simultaneously produced will have the opposite effect. At high temperatures mobile vacancies are present in metals in thermal equilibrium. In this case the cavities will absorb and emit vacancies until the internal gas pressure balances the surface energy of the cavity:

$$P_{eq}\, dv = \gamma\, da \qquad \text{or} \qquad P_{eq} = 2\gamma/R_c \qquad (13)$$

where v and a are the volume and surface area of a cavity and the surface tension γ is the energy per unit area to create new surface. This condition gives higher gas pressure and concentration of hydrogen in solution at smaller cavities than at larger cavities, leading to a net flow of hydrogen from smaller to larger cavities, i.e. to a coarsening of the cavity size distribution. The equilibrium gas pressure given by equation 13, which is the minimum for cavity growth, can be very high for small cavities. For example, a surface tension typical for metals of γ=1 joule/m^2, gives P_{eq} = 0.4 GPa (4 kilobar) for 10 nm diameter cavities. At this pressure the molar volume of hydrogen gas approaches that of solid materials and the equation of state departs significantly from ideal gas behavior [27]. When the gas pressure has the equilibrium value given by eq. 13 the forces on the cavity surface due to internal pressure and surface tension balance each other and there is no net stress in the lattice around the cavity.

In the absence of mobile vacancies the gas pressure in the cavities can rise above the value given by eq. 13 producing a stress field localized around each cavity. When the gas pressure is about an order of magnitude higher than the value given by eq. 13, cavity expansion through dislocation generation can occur [28].

The microstructure which results from precipitation of implanted hydrogen depends on the nucleation of cavities. If the implanted hydrogen and displacement defects are very mobile, their concentrations will remain low, the hydrogen chemical potential will

be low, and hydrogen precipitation is likely to occur only at pre-existing open volume sites such as grain boundaries or foreign inclusions. In this case, for low energy, i.e. shallow implantation, most of the hydrogen will escape from the surface and the fraction retained by precipitation into cavities will be small. If it is less mobile, the implanted hydrogen may build up to higher concentrations in solution in the implanted layer, giving a higher chemical potential which will eventually induce cavity nucleation. The production of displacement vacancies could assist initial nucleation and growth of cavities since agglomeration of vacancies along with trapping of hydrogen in them could create nuclei for gas precipitation. In this case a dense dispersion of very small cavities may develop in the implanted layer and the fraction of implanted hydrogen retained in the material may be close to 100% initially. As the implanted dose increases, the content of hydrogen and volume fraction of cavities increases. When the volume fraction of cavities is high enough, typically about 0.3, they become interconnected. Hydrogen implanted in beryllium at temperatures below 500 K behaves this way [29]. If the implantation profile (P(x) in eq. 2) peaks beneath the surface, cavity coalescence will lead to blistering and exfoliation of the overlying layer. In a plasma-wall environment the broad distribution of energies and angles of incidence are likely to produce a hydrogen implantation profile which is highest at or very close to the surface. In this case, metals in which implanted hydrogen has low mobility and solubility will develop a surface layer with interconnecting porosity connected to the surface.

Hydrogen dissolves exothermically in some metals, and in this case high concentrations of hydrogen in solution can have low chemical potential and hence low equilibrium gas pressure. In such metals hydrogen precipitates as an ordered metal-hydride phase rather than as gas bubbles. In many cases the concentration of hydrogen in solution in thermodynamic equilibrium with the hydride phase can be approximated by

$$C_{eq} = C_{ho} \exp(-Q_h/kT) , \qquad (14)$$

where Q_h is the enthalpy of formation of hydride from the solution phase, and C_{ho} is a temperature independent prefactor. Hydride precipitation can be included in the transport equation (eq.2) through a source/sink term which incorporates the equilibrium concentration in solution (eq.14) and which stops the hydride dissolution and formation reactions when the local volume fraction of hydride phase reaches 0 or 1 respectively [3].

The system of coupled partial differential equations given by eqs. 2, 5, and 10 can readily be solved in most cases by discretizing the spatial coordinate and then propagating the resulting system of ordinary differential equations forward in time from a specified initial condition using an integrating algorithm for stiff problems [30]. Several computer codes implementing numerical solutions to the hydrogen transport equation have been developed [3, 31-34].

Analytical solutions to the hydrogen transport equation are possible for some important cases. Doyle and Brice [35,36] have developed an analytical formalism for evaluating the hydrogen inventory, recycle and permeation rate and recycle time, under steady state conditions where hydrogen is being implanted at flux Φ and depth R_p and release is controlled by diffusion and surface recombination. They introduce a dimensionless transport parameter

$$W=(R_p/D)(K_r/\Phi)^{1/2}, \qquad (15)$$

for second order release kinetics where K_r is the surface recombination coefficient. The flux of implanted hydrogen creates a concentration of hydrogen in solution at depth R_p given by $\Phi = -D\,\partial C_s/\partial x = -DC_s/R_p$ for diffusion-limited release or by $C_s=(\Phi/K_r)^{1/2}$ for surface recombination limited release. In each case a near-surface concentration of mobile hydrogen is established, in a time $\tau = R_p^2/D(1+1/W^2)$, from which hydrogen may diffuse beyond the implantation depth. One can then predict whether precipitation is likely based on equations 7, 8 and 14 above. Also the concentration of hydrogen in traps in equilibrium with C_s can be obtained from equation 4 if the trap concentration and binding enthalpy of hydrogen to the traps is known. In general, the amount of hydrogen in the material in solution, trapped and precipitated states will depend on the incident flux. This can lead to dynamic pumping effects where hydrogen accumulates in the material during implantation and is released after the implantation ceases.

Here we briefly discuss two special cases of trapping in a material with a uniform concentration of traps where the concentration of mobile hydrogen in solution near the surface is fixed at a value C_{ss}. In the first case the concentration of traps $C_T >> C_{ss}$ and trapping is strong such that the concentration of hydrogen in solution in equilibrium with the traps $C_{eq} << C_{ss}$ until the traps are nearly full. In this case the traps will be full at depths less than $x=(2DtC_{ss}/C_T)^{1/2}$ and empty at greater depths. Secondly, consider the

case where the trapping is weaker such that the fraction of occupied traps is still small in equilibrium with hydrogen in solution at concentration C_{ss}. In this case the traps may be considered as another type of solution site and the flux of diffusing hydrogen can be

expressed as $J = - D \partial C_s/\partial x = - D^* \partial C_s^*/\partial x$ (16)

with an effective diffusivity $D^* = D/[1+C_T/z \exp(-Q_t/kT)]$ (17)

and effective concentration $C_s^* = C_s + C_t = C_s [1+C_T/z \exp(-Q_t/kT)]$. (18)

The steady state rate of permeation of hydrogen through a slab of material is not affected by traps, however, the time to reach steady state and the inventory of hydrogen in the material does depend on the trapping.

Carbon

Hydrogen retention

Carbon differs from metals in the behavior of implanted hydrogen. Implantation of hydrogen into carbon creates broken carbon bonds where hydrogen can be strongly bound through the formation of C-H chemical bonds. At low doses hydrogen implanted into carbon is nearly all retained near its end of range. As the dose increases, the local hydrogen concentration increases until it reaches a saturation value which is about 0.4-0.5 H/C for carbon at room temperature. Additional hydrogen, implanted into a region already saturated, escapes. Release of the hydrogen occurs through molecular recombination at the depth of implantation and not by atomic diffusion through the saturated layer to the surface [39]. Figure 3 shows an example of this saturation behavior [40]. The areal density of implanted hydrogen retained in the carbon therefore depends on the dose and energy as shown in figure 4 as observed both by NRA and TDS measurements [40-42]. At low doses the non-reflected hydrogen is all retained. At high doses the H retention saturates at a value determined by the saturation concentration and the thickness of the saturated layer, and therefore on the incident energy of the hydrogen. Saturation of hydrogen retention also occurs in other materials which form strong covalent bonds with hydrogen, for example boron and silicon. Similar saturation of hydrogen retention is observed in metals at temperatures where the implanted hydrogen cannot diffuse. Retention of hydrogen isotopes from tokamak plasmas implanted into carbon components typically saturates at coverages near 10^{17} atoms/cm^2.

Codeposition

In a tokamak, physical and chemical sputtering will produce an outgoing flux of carbon atoms from carbon plasma-facing surfaces. In general, there will also be an incoming flux of carbon atoms. If the outgoing carbon flux exceeds the incoming flux the surface will undergo net erosion. In tokamaks the flux of energetic hydrogen onto such surfaces is usually high enough that the surface remains saturated with hydrogen as it erodes. In this case the hydrogen coverage remains constant. However, if the outgoing carbon flux is less than the incoming flux, net deposition of carbon occurs. The deposited carbon becomes part of the hydrogen saturated layer which now increases in thickness with time. This leads to a hydrogen coverage which increases linearly with exposure time. This process, often referred to as codeposition, is the dominant process for long-term retention of hydrogen isotopes in tokamaks with carbon plasma-facing components.

Thermal release

The concentration at which H retention saturates decreases when the carbon is at higher temperatures during the implantation [39,42,43] as shown in figure 5. Figure 5 also shows the thermal release, due to isochronal annealing, of deuterium implanted into carbon at room temperature. Thermal release of implanted H begins around 800K. Measurements of D retention by NRA and by thermal desorption show similar dependence of deuterium retention on temperature of implantation [42], confirming that the fraction of D retained beyond the range of the NRA analysis (~1 μm) is small. This is consistent with localized D retention in the implanted region as shown in figure 3.

Isotope exchange

Experiments have shown that one isotope of hydrogen implanted to saturation into carbon can be displaced by subsequent implantation with another isotope [43-46]. The implanted hydrogen competes locally with other hydrogen atoms already present for the limited trap sites. In saturation the total incoming and outgoing fluxes are equal, but the isotopic mixture of the outflux is determined by the hydrogen isotopic composition of the saturated layer, not by that of the influx. This isotope exchange has been modeled by local mixing [45] or local recombination [39,47] models. In tokamaks with large areas of carbon facing the plasma, this isotope exchange process strongly impacts plasma

composition when the injected isotope is abruptly switched, for example from deuterium to tritium. Initially, tritium injected into the plasma is implanted into deuterium-saturated carbon surfaces where it exchanges with deuterium which flows back into the plasma. Since the inventory of deuterium in the wall is much larger than the amount in the plasma, it takes many discharges for the plasma to become mainly tritium. Similarly, tritium in saturated layers on plasma-facing surfaces, may be replaced with deuterium by deuterium fueled plasma operation. This is one method of reducing in-vessel tritium inventory.

Ion-induced release

Energetic particle bombardment also causes release of hydrogen from carbon by processes other than isotope exchange. Carbon implanted to saturation with hydrogen releases hydrogen when bombarded by non-hydrogenic ions such as helium or carbon, even when the ions are sufficiently energetic to pass through the saturated layer [47-50]. Fundamental mechanisms involved in ion-induced release are not well understood, but the process can be modeled by a transport equation with a fixed concentration of saturable traps including terms for trapping, thermal detrapping, an ion-induced detrapping rate which depends on the energy deposited into atomic collisions by the bombarding particles and local molecular recombination followed by rapid escape of the molecules possibly via interconnected microporosity [39, 47. 49, 51, 52].

In many cases, wall conditioning procedures used to control fuel recycling in tokamaks can be understood in terms of ion-induced release of hydrogen from plasma-facing carbon surfaces. Helium discharge conditioning or high power low density helium fueled plasmas are often used to remove hydrogen from the wall. After such conditioning the hydrogen content of the wall is below saturation and the wall has capacity to retain or pump incident energetic hydrogen until it again becomes saturated. Retention of charge-exchange neutrals over large areas by this mechanism reduces neutral density at the plasma edge. The wall pumping capacity can be large and persist for many shots since moderate particle fluxes over large areas are involved.

Bulk transport

The issues of bulk trapping of hydrogen and permeation of hydrogen into graphite beyond the range of implantation, have also been examined. The permeation depends

strongly on the microstructure of the graphite. In high density pyrolytic graphite there is very little permeation of hydrogen [53]. Some studies conclude that short-range atomic diffusion of hydrogen through the graphite lattice occurs at high temperatures (>1000 C) mainly along the basal planes [53-55]. At these high temperatures, graphite may also chemically react with hydrogen to form hydrocarbons.

Nuclear graphites, such as POCO AXF-5Q, are very inhomogeneous at submicron scales, and highly porous. Hydrogen implanted into such material at temperatures high enough for it to diffuse through the graphite lattice, must rapidly encounter microporosity or crystallite boundaries where it will exit the graphite lattice. Long range transport due to bulk concentration gradients is unlikely to occur in such inhomogeneous materials. The observed uptake of hydrogen into porous nuclear graphites from low energy plasmas, can be accounted for by thermally activated atomic diffusion along internal surfaces of pores and grains within the material which gives retained concentrations on the order of 10 atomic parts per million [47, 53].

Trapping

In a reactor, fusion neutrons will cause atomic displacements in graphite which may create traps for tritium. Trapping of hydrogen at lattice defects was therefore investigated in a series of experiments in which graphite was first irradiated with carbon ions to create traps, and then exposed to deuterium gas at 1200 C to decorate the traps with deuterium [55-59]. Irradiation produced strong traps, with binding energies consistent with C-H bond formation (~4.5 eV), and whose concentration saturated at about 1000 atomic parts per million (appm) at damage levels above about 1 displacement per carbon atom. For comparison, the concentration of strong traps in graphites as manufactured, i.e before ion irradiation , was typically in the range from 10 to 20 appm. An H451 graphite sample damaged by neutron irradiation had about the same D retention as graphite damaged by carbon ion irradiation.

Carbon plasma-facing surfaces retain energetic hydrogen from the plasma until they become saturated, after which the incident hydrogen is released as molecular hydrogen back into the plasma. This dynamic wall inventory strongly affects plasma fueling but contributes little to long term tritium inventory, which is mainly determined by codeposition of tritium with carbon. Hydrogen may penetrate into porosity in nuclear

graphites, but the retained concentration from this is too small to impact total hydrogen retention in current tokamaks.

Figure 6 illustrates several of the retention mechanisms discussed in this section. This figure shows deuterium retention on two DiMES probes exposed to the outer strike-point plasma in DIII-D [60]. Metal films approximately 100 nm thick were deposited on 8x8 mm square regions on the probe surfaces prior to exposure. One probe had tungsten and beryllium films and the other had molybdenum and vanadium films. Regions of graphite remained between the metal films. The probes were exposed to ELM-free quiescent H-mode conditions for 14 seconds for the Mo/V sample and 4 seconds for the W/Be sample. Deuterium ion fluxes estimated from Langmuir probe measurements were about 10^{18} D/cm^{2}s, thus the D fluences were sufficient to saturate retention on both probes. Net carbon erosion up to a few nanometers per second was measured on these probes, so the D retention is mainly due to implantation rather than codeposition. The carbon and Be show D retention consistent with implantation to saturation in materials where the implanted D is not mobile. The carbon has retained about $1.2\text{x}10^{17}$D/cm^2, indicating an incident D energy of about 300 eV (see fig. 5) and giving a saturate layer about 20 nm thick. The areal density of D in Be is slightly less than in carbon, consistent with the slightly lower saturation concentration for D implanted into Be. The much lower D retention in Mo and W is expected since the fast diffusion and low solubility of D in these materials allows the D to diffuse to the surface and escape. In vanadium, the fast diffusion and exothermic solubility cause the implanted D to precipitate into the hydride phase, resulting in higher D retention than in carbon, to depths beyond the range of implantation.

Sandia is a multiprogram laboratory operated by Sandia Corporation, a Lockheed Martin Company, for the United States Department of Energy under contract DE-AC04-94AL85000.

References

1. W. Möller and J. Roth, Physics of Plasma-Wall Interactions in Controlled Fusion, Eds. D. E. Post and R. Behrisch, NATO ASI Series B:Physics Vol 131, Plenum Press, New York (1986) p 439.
2. K.L. Wilson, R. Bastasz, R. A. Causey, D. K. Brice, B. L. Doyle, W. R. Wampler, W. Moller, B. M. U. Scherzer and T. Tanabe, Atomic and Plasma-Material Interaction Data for Fusion, Vol. 1, Supplement to the journal Nuclear Fusion, IAEA, Vienna, (1991) p 31.
3. S. M. Myers, P. M. Richards, W. R. Wampler, and F. Besenbacher, J. Nucl. Mater. **165** (1989) 9.
4. Handbook of Ion Implantation Technology, ed. J. Ziegler, North Holland, Amsterdam (1992).
5. W. Eckstein, Atomic and Plasma-Material Interaction Data for Fusion, Vol. 1, Supplement to the journal Nuclear Fusion, IAEA, Vienna, (1991) p 17.
6. J. F. Ziegler, J. P. Biersack and U. Littmark, The Stopping and Range of Ions in Solids, Pergamon Press, New York, (1985).
7. W. Eckstein, Computer Simulation of Ion-Solid Interactions, Springer Series in Materials Science Vol. 10, Springer-Verlag, Berlin (1991).
8. L. LeBlanc and G.G.Ross, Nucl. Instr. and Meth. **B83** (1993) 15.
9. H. Wipf, Diffusion of Hydrogen in Metals, in Hydrogen in Metals III, Springer Topics in Applied Physics Vol. 73, Springer-Verlag, Berlin (1997) p 51

9a. G. V. Kidson, The Diffusion of H, D and T in Solid Metals, in Landolt-Bönstein Numerical Data and Functionall Relationships in Science and Technology Group III: Crystal and Solid State Physics, Vol. 26 Diffusion in Solid Metals and Alloys, Springer-Verlag, Berlin (1990) p 504.

10. W. R. Wampler, J. Appl. Phys. **69** (1991) 3063.
11. M. A. Pick and K. Sonnenberg, J. Nucl. Mater. **131** (1985) 208.
12. M. I. Baskes, J. Nucl. Mater. **92** (1980) 318.
13. Wampler, J. Appl. Phys. **65** (1989) 4040 and J. Appl. Phys. **69** (1991) 3063.
14. S. M. Myers, P. Nordlander, F. Besenbacher ant J. K. Nørskov, Phys. Rev. **B33** (1986) 854.
15. H. Eleveld and A. van Veen, J.Nucl. Mater. **191-194** (1992) 433
16. J. R. Fransens, M. S. Abd El Keriem and F. Pleiter, J. Phys. Condens. Matter **3** (1991) 9871.
17. P. Nordlander, J. K. Nørskov and F. Besenbacher, J. Phys. F: Met. Phys. **16 (1986) 1161.**

18. J. K. Nørskov, Phys. Rev. **B26** (1982) 2875.
19. J. K. Nørskov and F. Besenbacher, J. Less Comm. Met. **130** (1987) 475
20. S. M. Myers et. al. Rev. Mod. Phys. **64** (1992) 559.
21. H. Katsuta, R. B. McLellan and K. Furukawa, J. Phys. Chem. Solids **43** (1982) 533.
22. R. Frauenfelder, J. Vac. Sci. Technol. **6** (1969) 388.
23. S. M. Myers and F. Besenbacher, J. Appl. Phys. **60 (1986) 3499.**
24. M. Y. Chou, P. K. Lam and M. L. Cohen, Phys. Rev. **B28** (1983) 4179.
25. V. I. Shapovalov and Yu. M. Dukelskii, Russ, Metall. **5** (1988) 210.
26. S. M. Myers and D. M. Follstaedt, J. Nucl. Mater. **145-147** (1987) 322.
27. H. Hemmes, A. Driessen and R. Griessen, J. Phys. C: Solid State Phys. **19** (1986) 3571.
28. G. W. Greenwood, A. J. E. Foreman and D. E. Rimmer, J. Nucl. Mater.**4** (1959) 305.
29. V. N. Chernikov, K. Kh. Alimov, A. V. Markin and A. P. Zakharov, J. Nucl. Mater **228** (1996) 47.
30. A.C. Hindmarsh, in Scientific Computing, Ed. R. S. Stepleman (North Holland, Amsterdam 1983) pp 55-64.
31. M. I. Baskes, Rep. SAND83-8231, Sandia National Laboratories, Albuquerque, NM (1983).
32. W. Möller, Rep. IPP-9/44, Max-Planck-Institut für Plasmaphysik, Garching (1983).
33. D. F. Holland and B. J. Merrill, in Engineering Problems of Fusion Research (Proc. 9th Symp. Chicago, 1981), IEEE, New York (1981) 1209.
34. F. Scaffifi-Argentina et.al. Fus. Tech. **32** (1997) 179.
35. B. L. Doyle and D. K. Brice, Rad. Eff. **89** (1985) 21.
36. B. L. Doyle, J. Nucl. Mater. 111-112 (1982) 628.
37. P. W. Tamm and L. D. Schmidt, J. Chem. Phys. **54** (1971) 4775.
38. T. U. Nahm and R. Gomer, Surface Science, **375** (1997) 281.
39. W. Möller, J. Nucl. Mater. **162-164** (1989) 138
40. W. R. Wampler, D. K. Brice and C. W. Magee, J. Nucl. Mater. **102** (1981) 304.
41. G. Staudenmaier et.al. ,J. Nucl. Mater. **84** (1979) 149.
42. A. A. Haasz and J. W. Davis, J. Nucl. Mater. **232** (1996) 219.
43. B. L. Doyle, W. R. Wampler and D. K. Brice, J. Nucl Mater. **103/104** (1981) 513.
44. W. R. Wampler and C. W. Magee, J. Nucl. Mater. **103/104** (1981) 509.
45. B. L. Doyle, W. R. Wampler, D. K. Brice and S. T. Picraux, J. Nucl Mater. **93/94** (1980) 551.

46. W. Möller, P. Børgesen and B. M. U. Scherzer, Nucl. Instr. and Meth. **B19/20** (1987) 826.

47. A. A. Haasz, P. Franzen, J. W. Davis, S. Chiu and C. S. Pitcher, J. Appl. Phys. **77**(1995) 66.

48. J. Roth, B. M. U. Scherzer, R. S. Blewer, D. K. Brice, S. T. Picraux and W. R. Wampler, J. Nucl. Mater. **93/94** (1980) 601.

49. W. R. Wampler and S. M. Myers J. Nucl. Mater. **111/112** (1982) 616.

50. W. R. Wampler, and B. L. Doyle, J. Nucl. Mater. **162/164** (1989) 1025.

51. R. A. Langley, J. Nucl. Mater. **162/164** (1989)1030.

52. D. K. Brice, Nucl. Instrum. Methods, **B44** (1990) 302.

53. R. A. Causey, J. Nucl. Mater. **162/164** (1989) 151.

54. K. N. Kushita, I. Youle, A. A. Haasz and J. A. Sawicki, J. Nucl. Mater. **179/181** (1991) 235.

55. V. N. Chernikov, W. R. Wampler, A. P. Zakhaorv and A. E. Gorodetsky, J. Nucl. Mater. **264** (1999) 180.

56. W. R. Wampler, B. L. Doyle, R. A. Causey and K. Wilson, J. Nucl. Mater. **176/177** (1990) 983.

57. V. N. Chernikov, A. E. Gorodetsky, S. L. Kanashenko, A. P. Zakharov, W. R. Wampler and B. L. Doyle, J. Nucl. Mater. **217** (1994) 250.

58. V. N. Chernikov, A. E. Gorodetsky, S. L. Kanashenko, A. P. Zakharov, W. R. Wampler and B. L. Doyle, J. Nucl. Mater. **220/22** (1995) 921.

59. S. L. Kanashenko, A. E. Gorodetsky, V. N. Chernikov, A. V. Markin, A. P. Zakharov, B. L. Doyle, and W. R. Wampler, J. Nucl. Mater. **233/237** (1996) 1207.

60. W. R. Wampler, R. Bastasz, D. Buchenauer, D. Whyte, C. P. C. Wong, N. H. Brooks and W. P. West, J. Nucl. Mater. **233/237** (1996) 791.

Table 1
Binding enthalpies (eV) of hydrogen to vacancies in metals.
Sources for values not referenced here are given in reference 3.

Metal	Experiment		Effective medium theory
	Internal redistribution	Positron annihilation	
Al	0.52	0.53	0.52
Fe	0.63		0.83
Ni	0.44	0.58, 0.44	0.52
Cu	0.42	≥ 0.4	0.37
Zr	0.28		
Mo	1.03	1.4	0.96
Pd	0.23		0.16
Ta	0.42	≤ 1.2	
W	1.04 [a]	1.16 [b]	1.15 [17]

[a] Thermal desorption [15]
[b] Perturbed angular correlation [16]

Table 2
Binding enthalpies (eV) of hydrogen to helium bubbles in metals.
Sources for values not referenced here are given in reference 3

Metal	Experiment		Effective Medium Theory	Chemisorption minus solution enthalpy
	Internal Redistribution	Gas phase equilibration		
Al	≤ 0.52		0.52	
Fe	0.78	0.81	0.91	0.73
Ni	0.55	0.52	0.66	0.6
Mo	1.15		0.98	1.3
Pd	0.29		0.35	0.35-0.43
Ta	0.53		0.69	
stainless steel	0.42			
inconel	0.45			
W			1.15 [17]	1.8 [22,40,41]

Figure Captions

1. Potential energy diagram for hydrogen in tungsten. Enthalpy of solution Q_s=1.04 eV [22], activation energy for diffusion E_m=0.39 eV [22], binding enthalpy of hydrogen to a vacancy Q_t=1.1 eV [15,16], enthalpy of adsorption Q_a=0.7 eV [37,38]. The activation energy for detrapping is Q_t+E_m.
2. The binding energy of a hydrogen or helium atom in a homogeneous electron gas as a function of average electron density in units of electrons/a_o^3 where a_o is the Bohr radius.
3. Depth profiles measured by SIMS of deuterium implanted at 530 and 1500 eV into carbon at room temperature at fluences of 10^{18} D/cm^2 (solid lines) and 10^{16} D/cm^2 (dotted curves). For comparison the low dose curves are scaled up by a factor of 100 [40].
4. Areal density of implanted deuterium retained in carbon versus incident fluence for different energies, measured by NRA (symbols) and calculated (curves) using implantation profiles and a saturation concentration of D/C=0.44 [40].
5. Relative D retention in carbon versus temperature measured by NRA. Squares show D retained after implantation at room temperature to doses of 10^{16}D/cm^2 (open) and 10^{18} D/cm^2 (filled) followed by five minute anneals at each temperature. The circled dots show relative retention of D implanted to saturation at the indicated temperature [43].
6. Deuterium retention on two DiMES samples with regions covered by metal films (indicated by horizontal bars), after exposure to the outer strike-point plasma in DIII-D. Regions between the metal films are graphite.

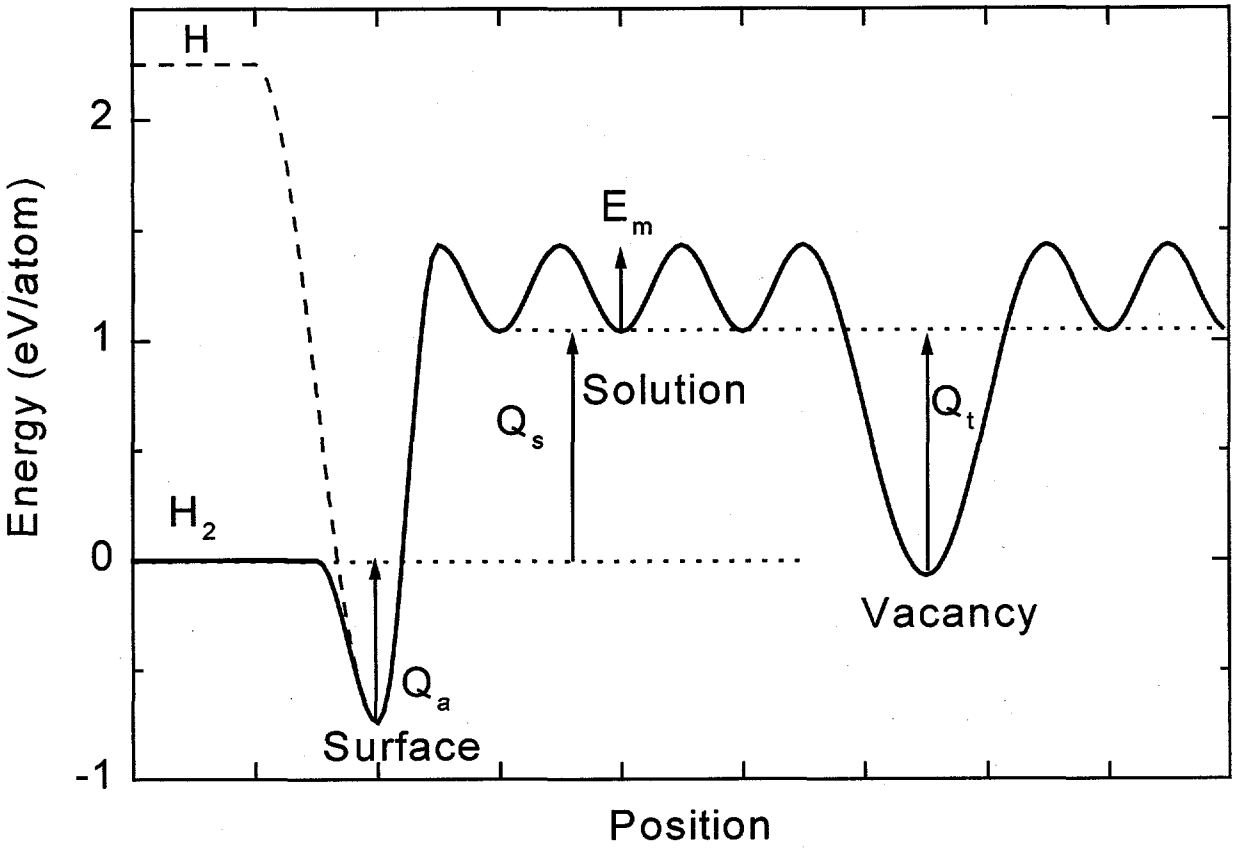
H
2
1
0
-1
Energy (eV/atom)
E_m
Solution
Q_s
Q_t
H_2
Q_a
Surface
Vacancy
Position

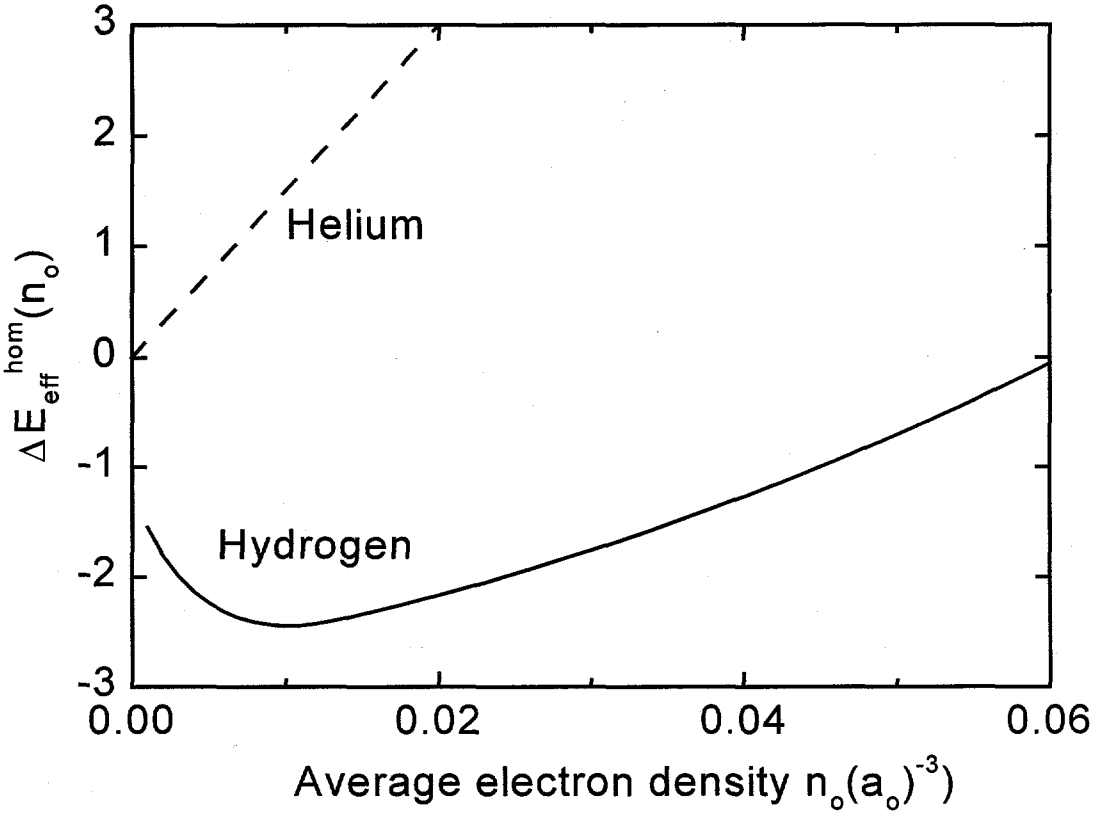
3
2
1
0
-1
-2
-3
0.00
0.02
0.04
0.06
Helium
Hydrogen
$\Delta E_{eff}^{hom}(n_o)$
Average electron density $n_o(a_o)^{-3}$)

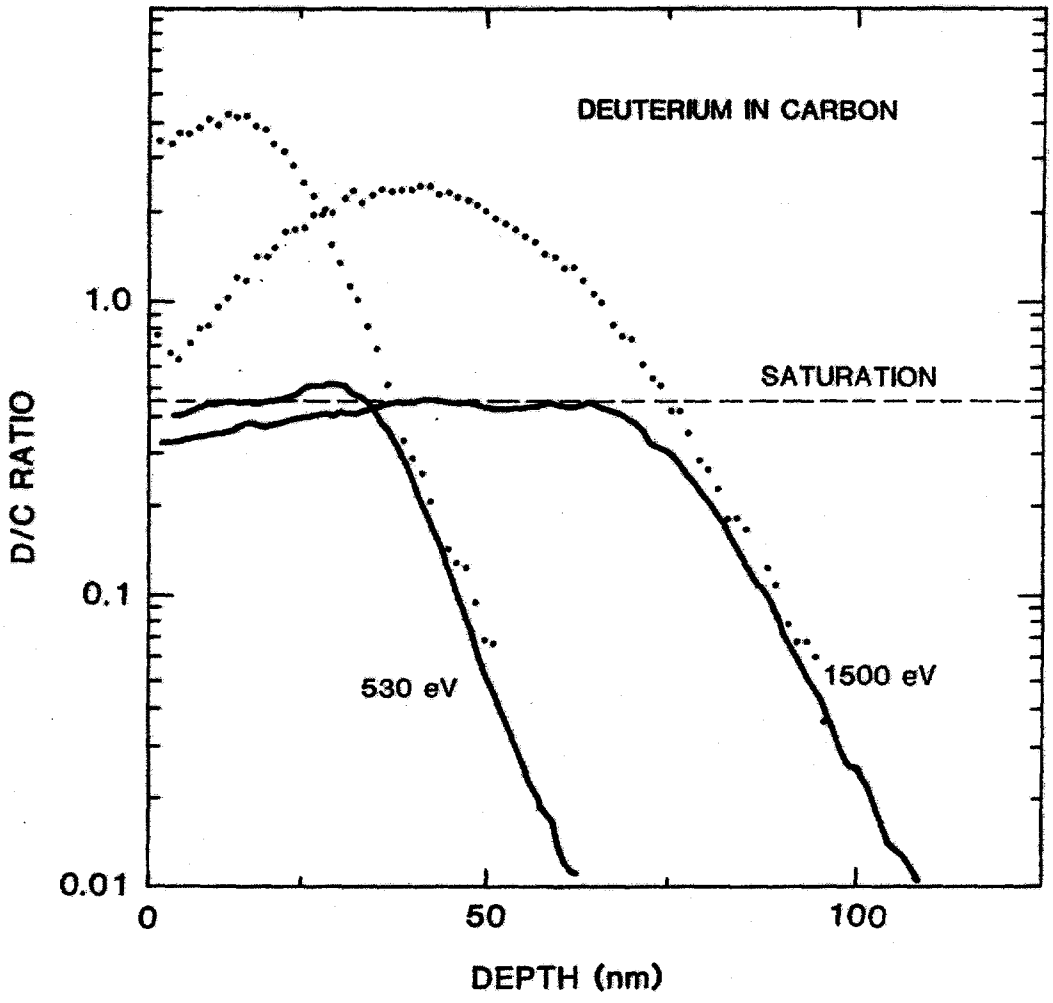
DEUTERIUM IN CARBON
SATURATION
530 eV
1500 eV
D/C RATIO
1.0
0.1
0.01
0
50
100
DEPTH (nm)

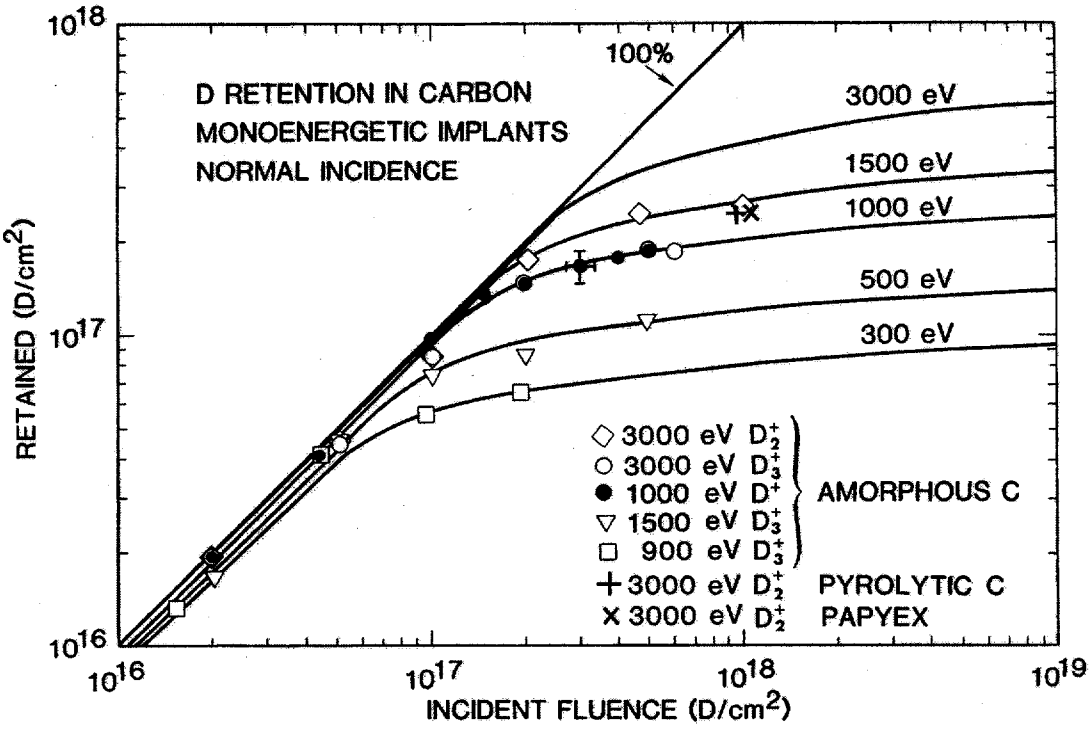
D RETENTION IN CARBON
MONOENERGETIC IMPLANTS
NORMAL INCIDENCE
100%
3000 eV
1500 eV
1000 eV
500 eV
300 eV
◇ 3000 eV D_2^+
○ 3000 eV D_3^+
● 1000 eV D^+
▽ 1500 eV D_3^+
□ 900 eV D_3^+
AMORPHOUS C
+ 3000 eV D_2^+ PYROLYTIC C
× 3000 eV D_2^+ PAPYEX
RETAINED (D/cm^2)
INCIDENT FLUENCE (D/cm^2)
10^{16}
10^{17}
10^{18}
10^{19}

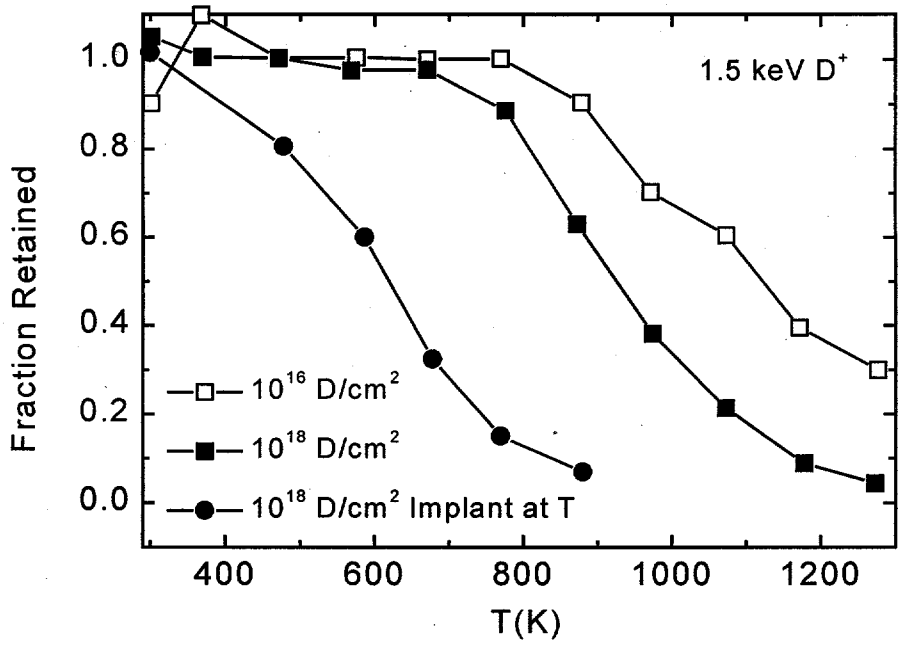
1.5 keV D+
Fraction Retained
1.0
0.8
0.6
0.4
0.2
0.0
10^16 D/cm^2
10^18 D/cm^2
10^18 D/cm^2 Implant at T
400
600
800
1000
1200
T(K)

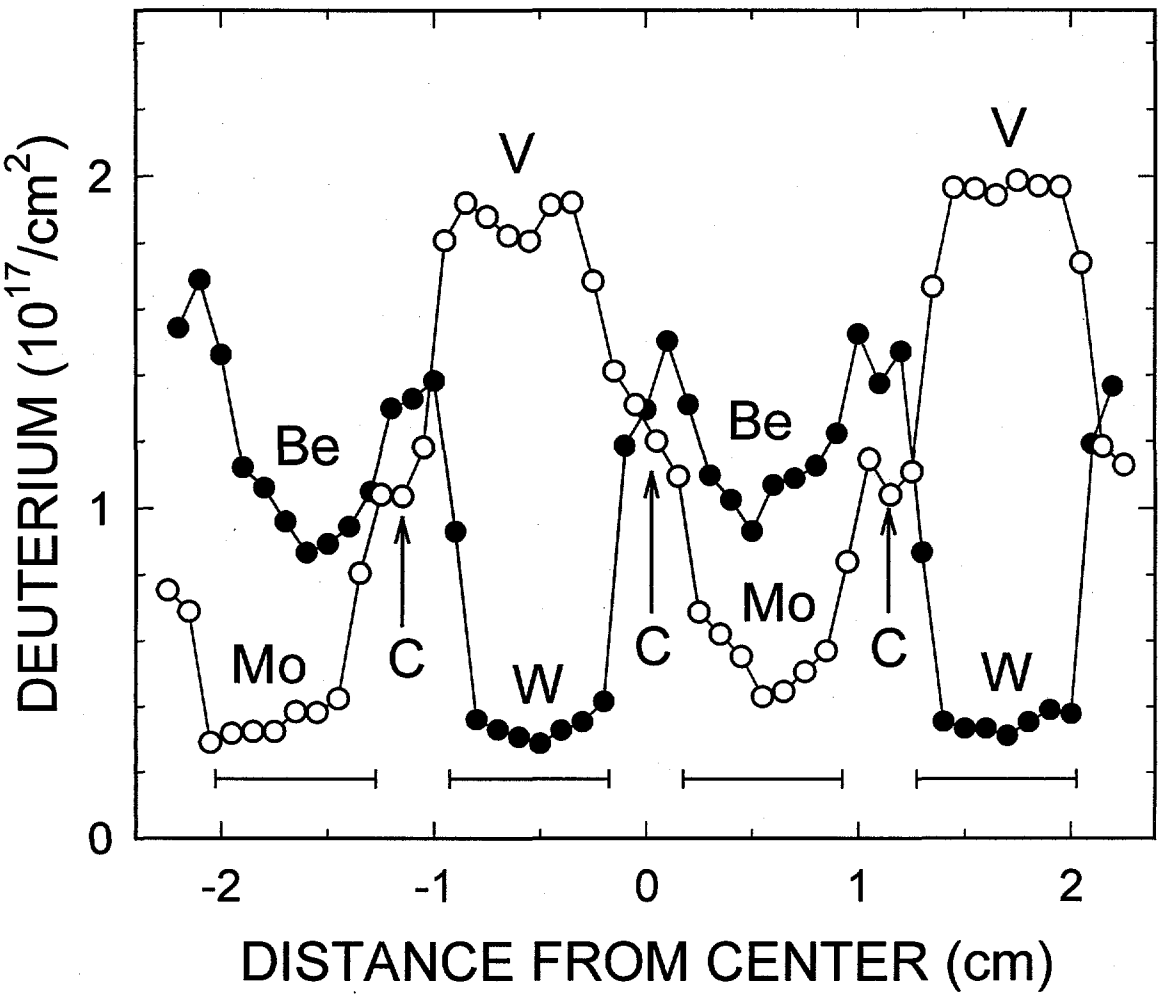
DEUTERIUM (10^{17}/cm^2)
0
1
2
-2
-1
0
1
2
DISTANCE FROM CENTER (cm)
V
V
Be
Be
Mo
Mo
C
C
C
W
W

Issues Arising from Plasma-Wall Interactions in ITER-Class Tokamaks

5.5.2.1 Deuterium Retention in Tokamaks.

The long-term accumulation of deuterium has been examined in several tokamaks through measurements of deuterium on plasma-facing components. These studies of long-term deuterium accumulation in tokamaks are reviewed in this section.

TFTR

In-vessel tritium inventory was a major concern for DT plasma operation in TFTR because of the 2 gram administrative limit on in-vessel tritium inventory. Prior to tritium fueled plasma operation there was an extensive evaluation of the anticipated in-vessel tritium inventory and the constraints this would impose on the TFTR DT experimental program. To establish a basis for predicting future tritium inventory, the in-vessel inventory of deuterium was followed from 1986 through 1991. The deuterium inventory was estimated from in-vessel surveys and analysis of components, including wall coupons and limiter tiles removed after each major run campaign. The deuterium inventory was also independently estimated from the fuel balance or net difference between the amounts of deuterium used to fuel the plasmas and deuterium recovered by the vessel pumping system.

An initial comprehensive study of D retention was done following the operational period from November 1985 to July 1987 [1, 2]. During this period TFTR produced 9922 high power plasmas with nearly circular cross section. The plasma boundary was defined by contact with a limiter of graphite tiles on the inner wall subtending poloidal angles from 60° below to 60° above the midplane with a total area of 22 m^2. The base temperature of first-wall components in TFTR was normally about 50°C, however the surface temperature rose during the discharge, with hot spots up to 800°C or higher. Following this period, in-vessel measurements of metal deposition on the limiter were made using beta backscattering [3]. The beta backscattering measurements provided a global picture of the pattern of metal deposition over the entire limiter. Figure 5.5.2.1-1 shows the beta backscattering map of metal deposition on one sector of the limiter. The map reveals regions of low metal deposition at the lower right and upper left, corresponding to regions of net erosion, and areas of high metal deposition in the upper right and lower left. This pattern was repeated on each of the 20 toroidal sectors of the limiter and could be observed visually as differences in the intensity of reflected light. This pattern of erosion and deposition results from the fact that each toroidal sector is slightly closer to the plasma at the center than at the sides [4, 5]. The regions undergoing net erosion were also observed to be the regions receiving the highest heat and ion fluxes [5, 6]. The beta backscattering showed net erosion occurring over approximately one third of the limiter area and net deposition over the remaining two thirds.

A large number of limiter tiles and wall coupons were removed for analysis. In addition, a large number of stainless steel clips, used to attach getter pumping panels to the outer wall, were removed and analyzed for deposited carbon and deuterium. These components sampled a broad range of poloidal and toroidal locations on the limiter and wall. The metal atom areal density on the limiter tiles measured by proton induced x-ray emission agreed with the metal coverage determined by beta backscattering. In addition, the areal density of deuterium on the limiter tiles, wall coupons and clips was measured by nuclear reaction analysis (NRA). The NRA method used probes to a maximum range of about 2 milligrams/cm^2, corresponding to a depth of about 10 mm in fully dense graphite, which in most cases was sufficient to reach through the deposited layer. On the plasma facing surfaces of the limiter tiles, there was a close correlation between the areal densities of deuterium and metal atoms. This correlation is due to the fact that regions undergoing net erosion have the least metal and deuterium coverage, whereas in regions of net deposition the metal and deuterium coverage both increase as the thickness of the deposited layer increases. Optical and electron microscopy on limiter tiles showed a layer of deposited material up to tens of microns thick, with a large volume fraction of open porosity, on regions of net deposition but not on regions of net erosion [3]. Ion-beam analysis showed this deposited material was mainly carbon and deuterium but also contained several atomic percent of oxygen and about 1 at.% of metal atoms (Cr, Fe, Ni).

Thick layers of deposited material were also found on the sides of the limiter tiles [1,2]. The D coverage on the sides of the tiles decreased approximately exponentially with distance from the plasma-facing surface with a characteristic e-folding length of about 0.6 cm. The local D areal density on the tile sides reached values comparable to the plasma-facing surface on tiles from regions of the limiter undergoing net deposition. Tiles from regions of net erosion had much higher D deposition on the sides than on the plasma-facing surfaces as shown in figure 5.5.2.1-2. D retention in regions of net erosion was dominated by deposition in the gaps between tiles. This pattern of deposition shows that there is a flux of carbon atoms from the plasma onto the limiter. In regions where incident ions have the highest flux and energy, the outgoing flux of eroded carbon, exceeds the incoming flux of carbon resulting in net erosion of the surface. On surfaces with lower incident ion flux and on surfaces shadowed from direct ion flux such as in the gaps between tiles, the incoming flux of carbon exceeds the outgoing flux and net accumulation of carbon with deuterium occurs. In TFTR the deuterium deposited in the gaps between limiter tiles was a significant fraction of the total in-vessel inventory of deuterium.

A measurement was also made to look for permeation of deuterium into the bulk of the graphite far beyond the range of energetic implantation. The D concentration, measured by NRA, was less than 0.5 atomic ppm at a depth of 2 mm beneath the plasma-facing surface of a tile from the TFTR limiter near the midplane. This measurement shows that permeation

deep into the bulk graphite did not contribute significantly to the in-vessel inventory of deuterium in TFTR [1,2].

Ion-beam analysis of the wall coupons and the much larger number of stainless steel clips gave a detailed picture of deuterium and carbon deposition on the wall. Carbon atom areal density on the clips ranged from about $4x10^{17}$ to $4x10^{18}$ atoms/cm^2. The ratio of deuterium to carbon on the clips varied from about 0.1 to 0.4 with an average value of 0.33 close to the saturation value of 0.4 observed for deuterium implanted into carbon. This high D/C ratio indicates that the rate of D accumulation on the wall may be determined by the carbon deposition rate rather than by the flux of deuterium onto the wall. Deposition was fairly uniform toroidally but was several times higher at the top and bottom of the vessel than at the outer midplane. This pattern of deposition is reasonable since the carbon deposition should be heavier closer to the source of the carbon which is the graphite limiter on the inner wall. The average areal density of D retained on the clips ($5.2x10^{17}$D/cm^2) was very close to the average areal density of D on the wall coupons ($5.7x10^{17}$D/cm^2), indicating that the more limited sampling by the coupons still gave an accurate measurement of global D deposition on the wall.

The in-vessel inventory of deuterium in TFTR at the time of the July 1987 maintenance opening is summarized in the first row of table 5.5.2.1. The table shows the total D retained and the percentage of retained D on the plasma-facing surface of the bumper limiter, in the gaps between limiter tiles and on the wall. For comparison the table also shows the quantity of D used to fuel high-power plasmas during the 1985-1987 run period from gas puffing, neutral beams and pellet injection. Fueling does not include gas used for low-power discharge conditioning. The far right column shows the fraction of deuterium retained, (in-vessel inventory divided by fueling) which for this first period was 22%.

D retention in TFTR was closely followed from 1987 through 1991. Each year limiter tiles and wall coupons were removed and analyzed for deuterium accumulated during the preceding run period. Beta backscattering and ion-beam analysis showed that regions of net erosion and deposition on the limiter remained similar from year to year. Table 5.5.2.1 summarizes the deuterium inventory in TFTR determined from these studies and the corresponding plasma fueling during each run period [7]. Over the 5 year period a total of 33.6 grams of deuterium was retained in the vessel and a total of 83 grams of deuterium was used to fuel plasmas. Therefore, during this 5 year period 40% of the deuterium used to fuel plasmas remained inside the vessel. Of this retained deuterium, 47% was on the plasma-facing surface of the limiter, 15% was is the gaps between limiter tiles and 38% was on the remaining vessel wall. The D retention is also graphically illustrated in figure 5.5.2.1-3. Table 1 also indicates that the fraction of D retained depended on how the plasma was fueled. In the period preceding 1987, the plasma fueling was mainly by gas puffing which gave the lowest retained fraction, whereas in the periods preceding 1988 and 1990 the plasma fueling was mainly by neutral beam injection which gave the highest percentage of D retained. This

correlation suggests that the fraction of D retained is smaller for discharges fueled by gas puffing than for discharges fueled by neutral beam injection.

It was also observed that the fraction of D retained increased with increasing neutral beam heating power [8]. Figure 5.5.2.1-4 shows the fraction of D retained in TFTR measured after each run campaign (given in table 5.5.2.1-1) versus the average neutral beam heating power. Higher power input to the plasma appears to cause greater carbon erosion and thus more codeposition. Also the CII emission light increases with NBI power indicating a more intense interaction of the plasma with the limiter.

Deuterium retention in TFTR was also examined by fuel balance methods in which the quantity of deuterium injected into the plasmas as gas or neutral beams was compared with the quantity of deuterium recovered by the vessel pumping system [9]. These studies showed that after many similar ohmic deuterium plasmas a steady state condition was reached in which about 25% of the D input was recovered from the vessel. In deuterium neutral beam heated plasmas the fraction of D recovered was about 50 to 75%. Although the short-term D retention from fuel balance varied depending on recent operating history, on average the fraction of D retained was large, consistent with the D inventory estimated from component analysis. In contrast, fuel balance measurements on plasmas fueled with helium showed that the fraction of helium recovered was very close to 100%. The fact that the chemically inert helium is not retained indicates that chemical bonding is involved in deuterium retention.

The main conclusions from these studies of D retention in TFTR are as follows. The primary physical mechanism for long-term D retention was codeposition of deuterium together with carbon eroded from the limiter by the plasma. In the period from 1985 to 1991 a total of 33.6 grams of D was retained in the vessel which was about 40% of the D used to fuel plasmas. This D retention was consistent with results from fuel balance studies [9] and accurately predicted the long-term tritium retention observed during subsequent tritium plasma operation [10, 11].

DIII-D

Several sets of graphite tiles from the lower divertor of the DIII-D tokamak were analyzed for retained deuterium in the period from 1987 to 1990 after exposures ranging from 1000 to 5500 high power plasmas [12]. D coverage on the plasma-facing surfaces of the 1988, 1989 and 1990 tile sets showed a consistent pattern. The D retention was high near the inner strikepoint (ISP) and low near the outer strikepoint (OSP). D coverage on the sides of the tiles was also examined on the 1989 and 1990 tile sets. High D coverage was found on the sides of the tiles which decreased exponentially with distance from the plasma-facing surface with an e-folding length of about 5 mm. The amount of deuterium on the DIII-D

lower divertor from exposure to 2000 plasmas was estimated to be about 1 gram from the D analysis on the 1990 tile set. About 60% of this D was on the plasma-facing surfaces of the tiles and 40% was on the tile sides, i.e. in the gaps between tiles.

This pattern of long-term D retention was consistent with measured long-term erosion/deposition on the divertor as shown in figure 5.5.2.1-3. The surface profile of the 1990 tile set was measured to an accuracy of ±1μm before and after exposure to the plasmas. These measurements showed a net erosion of about 5μm near the OSP and net deposition of about 5μm near the ISP [13] from exposure to 2000 plasmas. This long-term net erosion at the OSP is also consistent with erosion from short term exposures to well defined plasma conditions measured using the DiMES facility on DIII-D [14]. The picture which emerges from these studies is that net carbon erosion occurs from plasma-facing surfaces near the OSP where the fluxes of power and energetic particles are highest. D coverage remains relatively low on surfaces undergoing net erosion. The eroded carbon is redeposited in the gaps between tiles and onto plasma facing surfaces near the ISP where the plasma is often detached and the power flux and particle energies are lower than at the OSP. The redeposited carbon incorporates deuterium at concentrations of ~ 0.2 to 0.4 D/C. In regions of net deposition the areal density of deuterium therefore just depends on the thickness of the deposited layer. Erosion at the outer strikepoint and deposition at the inner strikepoint has been seen on several tokamaks [15].

Alcator C-Mod

In Alcator C-Mod the plasma contacting surfaces are molybdenum tiles. Erosion and deuterium retention might therefore be much lower than in tokamaks which have graphite as the main plasma contacting material. Measurements were made of erosion and deuterium coverage on the plasma-facing surfaces of a set of Mo tiles exposed to 1090 plasmas in C-Mod between November 1995 and March 1996 [16]. The average D coverage on tiles outside the divertor was $1.8\pm0.4 \times 10^{17}$ D/cm^2. The average D coverage on tiles inside the divertor was 1.0×10^{17} D/cm^2 on the inner strikeplate, 0.5×10^{17} D/cm^2 on the outer strikeplate, and 0.6×10^{17} D/cm^2 in the private flux region. Assuming the D coverage is toroidally symmetric these data give an in-vessel deuterium inventory of 0.10 gram outside the divertor and 0.0025 gram inside the divertor. These D coverages are much smaller than the D coverage found on graphite limiter and divertor tiles in TFTR and DIII-D.

Most of the C-Mod tiles analyzed in this study had a boron surface layer up to about a micron thick from boronization during the run campaign. Boronization is periodically applied in C-Mod because it reduces radiated power, which is primarily due to Mo impurities in the plasma, and dramatically improves H-mode performance [17]. The boron thickness is

much greater than the range of energetic D from the plasma, therefore the measured D retention is likely to be mainly due to implantation of D into the boron layer rather than into Mo. Retention of D implanted into boron is similar to that of D implanted into carbon. D is retained in the implanted layer until a saturation concentration is reached. The areal density of D retained after saturation depends on the thickness of the implanted layer and hence on the energy of the D. In tokamaks D retention by this mechanism should quickly saturate at an areal density in the range from about 1 - 3 x 10^{17} D/cm^2. The main difference between D retention in C-Mod and tokamaks with graphite divertors or limiters is that in C-Mod there was no significant accumulation of material redeposited by the plasma. The only region of net Mo erosion in C-Mod was near the outer strikepoint where ~ 0.15μm of net Mo erosion was measured and the surface boron layer was absent. Thus the quantity of eroded material is small.

The D depth profile measured by NRA on one of the tiles from the OSP, where the Mo surface was exposed to high D fluxes, gave an areal density of 6x10^{15} D/cm^2. Within the accuracy of the measurement this D was all within 0.1μm of the surface. The fraction of D at depths between 0.2 μm and the maximum depth probed (2 μm) was less than 10% of the total. This measurement shows that permeation of D into the Mo gives bulk concentrations less than 5x10^{-5} atom fraction which would not give a large in-vessel D inventory.

JET

Long term deuterium retention has been closely followed in JET since 1985 by analysis of components removed after each operational campaign [18, 19, 20, 21, 22]. These studies include periods of operation with limiter and with divertor plasma configurations, and with both carbon and beryllium first wall materials. By 1988 55% of the geometric surface area of the wall was covered with graphite or CFC tiles, including all surfaces exposed to ions traveling along field lines. The carbon components included tiles covering the inner wall, two toroidal belt limiters on the outer wall and 40 poloidal rings of carbon tiles. After the "all carbon" campaign completed in May 1988 the total long term D retention in the vessel from about 2500 plasmas was estimated, from hundreds of measurements of D on tiles and long term samples, to be 3.6 grams or about 17% of the D input during the campaign [19, 21]. About 1000 of these discharges were with the "X-point" open divertor configuration in which the upper X-point is positioned just inside the poloidal rings of tiles at the top of the vessel. On belt limiter tiles and X-point tiles regions of net erosion, with D coverage of ~ 10^{17} atoms/cm^2 , were seen at locations of highest incident power flux. On nearby surfaces with lower power flux there was net deposition of D with carbon. Most of the D inventory was associated with relatively small regions of deposited material. During this campaign the

mean daily retention of D in the vessel was estimated from fuel balance to be about 40% of the gas input [23]. The difference in retained fraction from fuel balance and component analysis is largely due to D removed during venting and He glow discharge cleaning, which was not included in the fuel balance analysis. Considering this, the D retention estimated by these two methods are in good agreement.

In 1989 beryllium was introduced into JET in two stages. First, Be was evaporated onto the entire inner wall, typically about 10 nm each night prior to running the following day, then a few months later the graphite toroidal limiter tiles were replaced with Be tiles. The introduction of Be did not significantly change the long term average quantity of D retained per pulse. Also, the distribution of long-term D retention within the vessel after operation with Be was similar to that for the "all carbon" phase of 1988 [21]. However, during operation with Be the amount of D required to fuel the plasmas increased by about a factor of 4 compared to fueling for "all carbon" operation [20, 21]. This increased fueling is due to a larger dynamic wall inventory, i.e. D which is absorbed by the wall during discharges and then released between discharges. These observations are consistent with the model [24] that the dynamic inventory is controlled by implantation of charge exchange neutrals into a thin surface layer over the entire vessel surface area, whereas long term D retention is dominated by codeposition of D with material eroded by the plasma from localized regions of high power flux (see the discussion of dynamic wall loading in section 6.4). Be evaporation changed the composition of the near surface layer from mainly carbon to Be over the entire vessel. Thus the different dynamic D inventory reflects the difference between C and Be in their ability to release implanted D between discharges. However, the thin evaporated Be film would be quickly removed from regions undergoing net erosion at locations of highest heat flux, leaving erosion and redeposition of the carbon, and hence long-term D retention, little affected by the Be evaporation.

To improve upper X-point open divertor operation, the top of the vessel was fully covered by carbon tiles early in 1992 and modifications to improve power loading were made in August 1992. The tile shapes provided shadowed regions on adjacent tiles so that no edges, would be exposed to excessive heat flux due to imperfect tile alignment. While in the vessel, these tiles were frequently coated with thin Be films of fairly uniform thickness from the sublimation sources. Analysis of D and Be coverage on these X-point tiles after the run campaign [19, 20, 21] revealed regions of net erosion, with low D and Be coverage, at locations of highest power flux at the inner and outer strikepoints. Areas of heavy net deposition with high coverage of D and Be were present on nearby regions of lower power flux, particularly near the inner strike zone and in the private flux region. Also, heavy deposition on shadowed surfaces in the strike zones show there was local redeposition of carbon from the plasma onto surfaces shadowed from ion flux.

JET operated with a toroidal divertor in the bottom of the vessel with CFC tiles from April 1994 to March 1995 and with Be tiles from April to June 1995. A cross-section of this

Mk I divertor is illustrated in figure 5.5.2.1-6a. Tiles were attached to a water cooled support so their ambient temperature was ~ 50°C. In contrast, all plasma-facing components had ambient temperatures of at least 300°C prior to installation of the Mk I divertor. Each divertor tile was inclined along the toroidal direction to shadow the edge and some of the surface (typically 15 to 50 %) of the adjacent tile to protect tile edges from excessive heat flux. After these two campaigns tiles were examined by nuclear reaction analysis for near-surface D, Be and C [22].

The most striking feature of the distribution of D on the carbon tiles is the heavy accumulation of D in the shadowed areas at the strike and scrape-off regions, i.e. on shadowed surfaces adjacent to regions of net erosion. Regions exposed to ion flux had low D coverage indicating net erosion. Also, the D coverage was much higher on the inner leg of the divertor than on the outer leg. Similar patterns of heavy deposition in shadowed areas were seen on the inner side wall tiles as on the inner floor tiles, but the outer side wall tiles had low coverage of D. Within the private flux zone D coverage was low both inside and outside the shadowed regions.

The amount and distribution of D on the Be tiles in the inner half of the divertor was similar to that for the graphite tiles, however, on the outer half of the divertor there was much less D retained on the Be than on the carbon tiles. Ion-beam analysis showed that the heavy deposits on the Be tiles were predominantly carbon and not beryllium and that the regions exposed to ion flux, i.e. of net erosion, were mainly beryllium with little carbon. This leads to the conclusion that even with a Be divertor D retention is largely due to codeposition with carbon transported into the divertor from the main chamber. For most of the discharges with the Be divertor the main plasma impurity was carbon, not Be. Furthermore, carbon must be redistributed by local recycling within the divertor until it reaches shadowed areas which act as sinks. The fact that these deposits are predominately carbon indicates that local recycling transports carbon more efficiently than Be.

Long-term samples exposed at the wall of the main plasma chamber to ~940 plasmas between April and June 1995 revealed net erosion of the surface [25]. Therefore codeposition of D on the main chamber wall would not contribute to long-term D retention. Instead, this result indicates that the main chamber wall is a source of impurities due to erosion by charge exchange neutral D. Graphite components in the main plasma chamber not fully covered by Be evaporation could thus be the source of carbon deposited onto the Be divertor.

The Mk IIA divertor was installed in JET for operation from April 1996 to February 1998. Its cross section is shown in figure 5.5.2.2.-6b. It was designed to be more closed than the Mk I divertor, which it replaced, and to exhaust particles through gaps between the floor and side wall modules at the inner and outer corners making it more like the ITER divertor design. Deuterium coverage was measured by NRA over a set of Mk IIA graphite floor tiles removed in October 1996 after ~ 2000 pulses. The D coverage was quite uniform toroidally.

D coverage was low ($<10^{18}/cm^2$) in the private flux region. The ends of tile 7, where D analysis was low ($<10^{18}/cm^2$) and tile 4 where D coverage was high ($>3x10^{19}/cm^2$) were shadowed from ion flux by the side wall tiles 8 and 3 respectively. There was also heavy deposition on the water cooled louvers beyond the inner corner and on the bottom end of side wall tile 3. In contrast, the shadowed region of tile 7 and the louver surfaces beyond the outer corner appear pristine. The outer side wall tiles also appear clean with D coverage of ~ $3x10^{17}/cm^2$, compared with an order of magnitude higher D coverage on the inner side wall. D retention in the Mk IIA divertor was dominated by codeposition with carbon beyond the inner corner of the divertor on the louvers and the tile surfaces adjacent to the pumping gap. The pattern of deposition indicated mainly line of sight transport from the strike zone or pumping gap many centimeters into regions shielded from ion flux. This indicates that the carbon is transported as neutral atoms or molecules. The films on surfaces facing the inner pumping gap were measured to be 40 μm thick and were seen to flake off from metal surfaces such as the louvers, probably on venting the vessel. Ion beam analysis of the flakes gave the D/C ratio of 0.4 [26]. It was estimated that this heavy codeposition inside the inner pumping gap resulted in additional long term retention of at least 6% of the gas fueling, and this also resulted in higher than expected retention of tritium during subsequent tritium fueled plasma experiments.

ASDEX-Upgrade

In the period between March 1991 to July 1995 ASDEX Upgrade operated with a lower single null plasma configuration with a divertor consisting of graphite tiles. During this time the divertor tiles were exposed to about 1900 plasmas. At the end of this period, divertor tiles were removed for analysis. Tungsten (W) coated graphite tiles were then installed in the divertor. In the period from December 1995 to July 1996 the W coated tiles were exposed to about 800 plasmas. At the end of this W divertor campaign, divertor tiles and components from the main plasma chamber were removed and analyzed. These two campaigns provide a unique comparison of low-Z versus high Z divertor material with similar geometry and plasma conditions. The divertor geometry during these campaigns is shown in figure 5.1.2.1-7 (AUG Div I).

The W coated tiles had a 500μm thick plasma sprayed layer of W on a graphite substrate and provided nearly full toroidal coverage of a region 16 cm wide at both the inner and outer strike points. These tiles were inclined toroidally to protect tile edges resulting in a region about 2 cm wide on each tile which was shadowed from ion flux. A wide array of analysis methods were used to determine the elemental composition of the near-surface region of the components. In particular, the deuterium content was examined using thermal desorption spectrometry (TDS), nuclear reaction analysis (NRA) and secondary ion mass spectrometry (SIMS) [27, 28, 29, 30].

For the graphite divertor tiles removed in 1995, the peak deuterium areal density was about $3x10^{19}$ D/cm^2 on the inner divertor and about a factor of two lower on the outer divertor [27, 28]. The deuterium was observed to be present in deposited material consisting mainly of carbon, boron, H and D of non-uniform thickness due to the roughness of the substrate [28]. The total amount of H and D in the graphite divertor tiles was estimated to be about $2x10^{24}$ atoms or about 6 grams [27].

On the W divertor tiles, the highest D areal density (~$5x10^{18}$D/cm^2) was measured in the shadowed region of the inner divertor outside the separatrix. The D areal densities on the W inner divertor plate were several times lower on the unshadowed regions than on the shadowed regions. On the outer W divertor plate the D areal densities were about ten times less than on the inner W divertor and were about the same in shadowed and unshadowed regions. In the case of the W divertor experiment, more than 50% of the total in-vessel D inventory was on the inner divertor while less than 10% was on the outer divertor [30]. The total amount of D retained on divertor tiles during the W divertor experiment was $1.0x10^{23}$ atoms (0.3 gram) [29] which is 20 times less, or about 8 times less per shot than during previous operation with a graphite divertor. Comparison with the quantity of D used to fuel the plasma during these periods, predominantly by gas injection, shows that with the W divertor about 2% of the D input was retained [29], whereas during previous operation with a graphite divertor the fraction of D retained was much larger [27].

With both the graphite and W divertors, the inner divertor was found to be completely covered by a layer of low Z material a few microns thick, whereas, on the outer divertor the deposition was discontinuous on the scale of the surface roughness[28, 30]. On the outer divertor deposited low-Z material was found in microdepressions of the rough surface which are shielded from re-erosion, whereas adjacent protruding parts of the rough surface undergo net erosion and were not covered by low Z material. The areal density of deposited low-Z atoms was about five times less on the outer divertor than on the inner divertor [30] , which is sufficient to accommodate the much lower areal density of retained D by codeposition. The similar distributions of deuterium and low-Z deposition shows that for both the graphite and W divertors the dominant mechanism for deuterium retention is codeposition of D with low-Z elements, mainly carbon and boron, onto the surface. Also, in general, deposition dominates on the inner divertor while erosion prevails on the outer divertor (see figure 5.1.2.1-7).

The D coverage was also measured on graphite plasma-facing components from the main plasma chamber following the W divertor experiment. These surfaces, which do not have direct plasma contact, had areal densities of 1-$2x10^{17}$ D/cm^2. The observed magnitude and poloidal distribution of this retained D is consistent with a model based on implantation of charge exchange neutrals from the plasma [30]. Even though the area is large, this mechanism does not dominate long-term D retention because retention by this mechanism saturates at a relatively low coverage due to the small thickness (<0.1μm) of the implanted layer.

The observations that the average quantity of D retained per shot, or fraction of D input retained, is about an order of magnitude smaller with the W divertor than with the graphite divertor, and that the D is mainly in regions of net deposition on the inner divertor, indicate that with the graphite divertor, D retention is mainly due to codeposition of D with carbon eroded from the outer divertor. By removing this major source of carbon erosion, the W divertor greatly decreased D retention with no adverse effects on plasma conditions.

In 1997 ASDEX upgrade began operation with a new divertor geometry (illustrated in figure 5.1.2.1-7 AUG Div II) which used CFC tiles. In this new geometry the strikepoints are on nearly vertical tile surfaces and the pumping slots are inside the strikepoints, i.e. in the private flux region. Local maxima in D coverage were observed at both the inner and outer strikepoints as shown in fig. 5.1.2.1-7. Plasma edge modeling indicates that for the Div I geometry the plasma electron temperature is high enough to cause erosion at the outer strikepoint but not at the inner strikepoint, whereas for the Div II geometry the electron temperature is below the threshold for erosion at both the inner and outer strikepoints [31].

Tore Supra

In Tore Supra a large fraction of plasma facing surfaces, are covered with graphite tiles [32]. This includes tiles on the inner wall which are often used as a limiter and which are actively cooled to accommodate long pulse operation. Controlling dynamic wall loading has been especially critical in Tore Supra due to the long discharge duration (see section 5.4). Removal of deuterium from the vessel either by He discharge preconditioning of the wall [33, 34] or with the ergodic divertor and pump limiters [35], are necessary to prevent density limit disruptions due to uncontrolled fueling of the plasma from the wall.

In 1992 carbon and silicon long term samples were exposed to 2333 discharges in Tore Supra [32]. These samples were located between tiles on the inner wall and were mounted with their surface at the same radial position as the tiles. After exposure the retained deuterium was measured by NRA using an analysis beam of 790 keV ^{3}He. At this energy NRA measures D within about 1 μm of the surface. The average D coverage was greater than 10^{18} D/cm^2 which gives a total in-vessel D inventory greater than 10^{24} atoms or 3.3 grams. Proton backscattering analysis of the silicon samples showed carbon deposits of about 10^{19} C/cm^2, or about 1 μm thick, on many of the samples. This carbon deposition, and the fact that the amount of retained D is much higher than can be reached by charge exchange implantation, lead to the conclusion that long term D retention in Tore Supra is mainly due to codeposition of D with carbon.

JT-60U

In JT-60U the wall is covered with tiles of graphite or CFC, some of which are coated with B_4C. JT-60U operates with a single lower open X-point divertor. Deuterium retention was examined on tiles which were exposed to 3170 plasmas between March 1991 and

October 1992 [36]. About 70% of these plasmas were deuterium fueled, the remainder, including the last 146 plasmas in this period, were hydrogen fueled. The tiles included a set spanning the divertor region. The coverage of deuterium was measured by NRA with an 800 keV ^{3}He analysis beam, which detects D within about 1μm of the surface. Figure 5.5.2.1-7 shows the D coverage across the divertor tiles [37]. The inset shows the location of the tiles relative to the strikepoints during the period the tiles were exposed. The lowest D coverage (~$3x10^{16}$ D/cm^2) is on tile f at the outer strikepoint while the highest D coverage (~$6x10^{17}$ D/cm^2) is on tiles c & d near the inner strikepoint . This is consistent with net erosion of carbon at the outer strikepoint and net codeposition of D with carbon near the inner strikepoint. The very low D coverage on tile f may also in part be due to the operation with H plasmas at the end of the run period.

Analysis of tritium in plasma-facing components and exhaust gases show that 50% or more of tritium produced by d(d,p)t nuclear reactions in the plasma, in the period between July 1991 and October 1993, remained inside the vessel [38] (see section 5.5.2.2).

TEXTOR

TEXTOR operates with a circular plasma whose boundary is determined either by an inner bumper limiter (IBL), or a toroidal belt limiter located 45 degrees below the outer midplane (ALT-II). Both limiters are constructed of graphite tiles. In March 1989 16 ALT-II tiles and 10 IBL tiles were removed from TEXTOR and analyzed for deposited metals and deuterium [39].

Discussion

In tokamaks with carbon plasma facing components, long term D retention is mainly due to codeposition of D with carbon. In divertor tokamaks this codeposition occurs mainly in the divertor. This occurs, even when the divertor strikepoint is not carbon as with the JET MkI beryllium divertor or the ASDEX-Upgrade tungsten divertor, where other plasma facing components act as sources of carbon to the plasma. In Alcator C-Mod which has no carbon plasma facing components, D retention is low and is mainly due to implantation of energetic D from the plasma and not by codeposition as shown by the low D retention in the C-Mod divertor. In divertor tokamaks, D retention on the wall of the main plasma chamber is about the level expected from implantation by energetic charge exchange neutrals from the plasma [30]. This main chamber wall inventory does not greatly contribute to long term deuterium inventory because the thickness of the implanted layer is small (<0.1 μm). However, the quantity of this D in the main chamber wall is much larger than the quantity of D in a plasma and the dynamic variations of this wall inventory dramatically impact fueling of individual discharges [24].

In several tokamaks the net erosion/ deposition and associated D retention is asymmetric with respect to the inner and outer strikepoints. This is the case in JET, DIII-D, ASDEX

Upgrade and Alcator C-Mod [15]. The outer strikepoint is generally a region of net erosion, whereas net deposition of carbon is seen on the inner divertor. Plasma modeling indicates this could be due to higher average electron temperatures in the outer divertor which gives more energetic ions onto the strikepoint and higher sputtering yields [30, 31].

A striking feature, which is seen in many tokamaks, is the intense codeposition of carbon and deuterium in regions which are shadowed from ion flux but are near carbon surfaces receiving high ion flux. Examples of this are surfaces facing the inner pumping port in the JET MkIIA divertor and regions shadowed by adjacent tiles (JET and ASDEX-Upgrade) and on the sides of tiles (TFTR and DIII-D). Since ions cannot reach these shadowed surfaces, this carbon deposition can only be due to neutral carbon atoms or molecules. In some cases these surfaces may have line of sight to a carbon surface receiving intense ion flux, where neutral atoms or molecules might originate. In other cases, where there is no line of sight to such surfaces, the neutral carbon must come from the boundary plasma. Sputtered atoms are unlikely to return to the surface as neutrals, instead they will be ionized and return to surfaces intersecting field lines. However, hydrocarbon molecules leaving the surface can be dissociated through impact by hot electrons in the plasma. Electron impact induced neutral dissociation or dissociative ionization of hydrocarbon molecules can yield energetic neutral fragments, including hydrocarbon radicals and atoms [40]. Examples of such reactions for methane are

$$e^- + CH_x \rightarrow e^- + CH_{x-1} + H \qquad \text{neutral dissociation}$$

or

$$e^- + CH_x \rightarrow 2e^- + CH_{x-1} + H^+ \qquad \text{dissociative ionization}$$

where x=1 to 4. These processes occur through a transition of the molecule to an excited electronic state whose energy exceeds the molecular binding energy. The excess electronic energy is converted to kinetic energy of the fragments. This process also produces energetic hydrogen atoms through the dissociation of molecular hydrogen at the boundary of fusion plasmas. Cross sections for production of CH_3 and CH_2 , by electron bombardment of methane, peak at electron energies between 20-30 eV [41] and in this energy range dissociation into neutrals, rather than dissociative ionization, is mainly responsible for the production of molecular radicals [42]. Furthermore, erosion of graphite from hydrogen impact occurs mainly through production of methane and heavier hydrocarbons for hydrogen energies below 100 eV, and these chemical erosion yields have been measured to be in the range of 10^{-2} C/H [43]. Therefore it is likely that carbon surfaces exposed to high fluxes of hydrogenic ions, such as divertor strikepoints will be a strong source of hydrocarbon molecules into the plasma. A large fraction of this carbon will promptly return to nearby surfaces as energetic neutral carbon or hydrocarbon radicals after undergoing electron impact dissociation in the boundary plasma. Chemical erosion followed by molecular dissociation will therefore result in intense recycling of neutral carbon and hydrogen back and forth between the plasma and the surface where carbon surfaces are exposed to high fluxes of hydrogen ions from the plasma, such as at divertor strikepoints. This process can account for

transport of carbon into regions shadowed from ion flux where it is then shielded from further erosion. In contrast, the same mechanism would not occur for metal atoms. Erosion due to chemical sputtering by hydrogen at low energies does not occur for metals [43]. Since metal atoms do not form strong molecular bonds with hydrogen, metals are eroded by physical sputtering as atoms, not as molecules. The important consequence of this for tokamaks is that the eroded metal atoms cannot redeposit locally as neutrals but will be ionized, confined by the magnetic field, and redeposit back onto surfaces intersecting field lines, i.e. where erosion is greatest. This would make the net erosion rate for metals smaller than that of carbon. The absence of chemical sputtering is another factor which reduces the erosion rate for metals. The ability of carbon but not metal atoms to redeposit in shadowed regions is consistent with the observation in JET that on the Mk I beryllium divertor the heavy deposits were predominantly carbon and not beryllium and that the regions exposed to ion flux, i.e. of net erosion, were mainly beryllium with little carbon. Beryllium and carbon would both be eroded from the plasma contacting regions, but only the carbon would be deposited as neutrals into the shadowed regions. This process might be used to advantage, to localize deposition of carbon in regions where it can be removed or heated to thermally release tritium.

Table 1 Deuterium retention and fueling in TFTR

Year	D Retained				D Fueling				%Retained
	total (gm)	% BL Face	% BL gap	% Wall	total (gm)	%gas	%NB	%pellet	
1987	5.3	50	11	39	24	76	18	6	22
1988	5.7	40	33	27	9	25	75	0	63
1989	7.3	57	13	30	18	38	47	15	41
1990	11	55	12	33	22	27	73	0	50
1991	4.3	18	8	74	10	40	60	0	43
Total	33.6	47	15	38	83	45	50	5	40

Sandia is a multiprogram laboratory operated by Sandia Corporation, a Lockheed Martin Company, for the United States Department of Energy under contract DE-AC04-94AL85000.

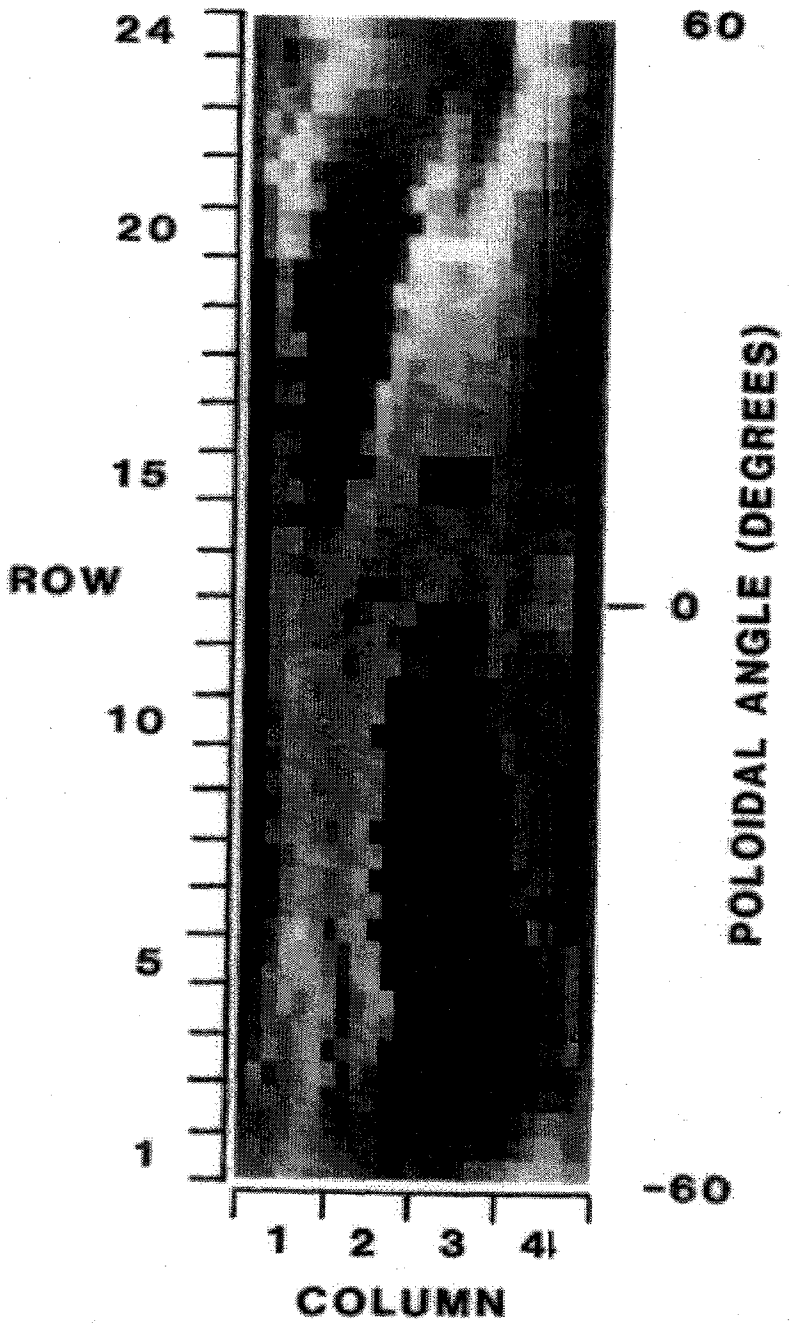

FIG. 5.5.2.1-1 The areal density of metal atoms on one sector of the TFTR limiter measured by beta backscattering. The highest metal atom deposition (lightest region in the figure) is ~ 10^{18} atoms/cm^2.

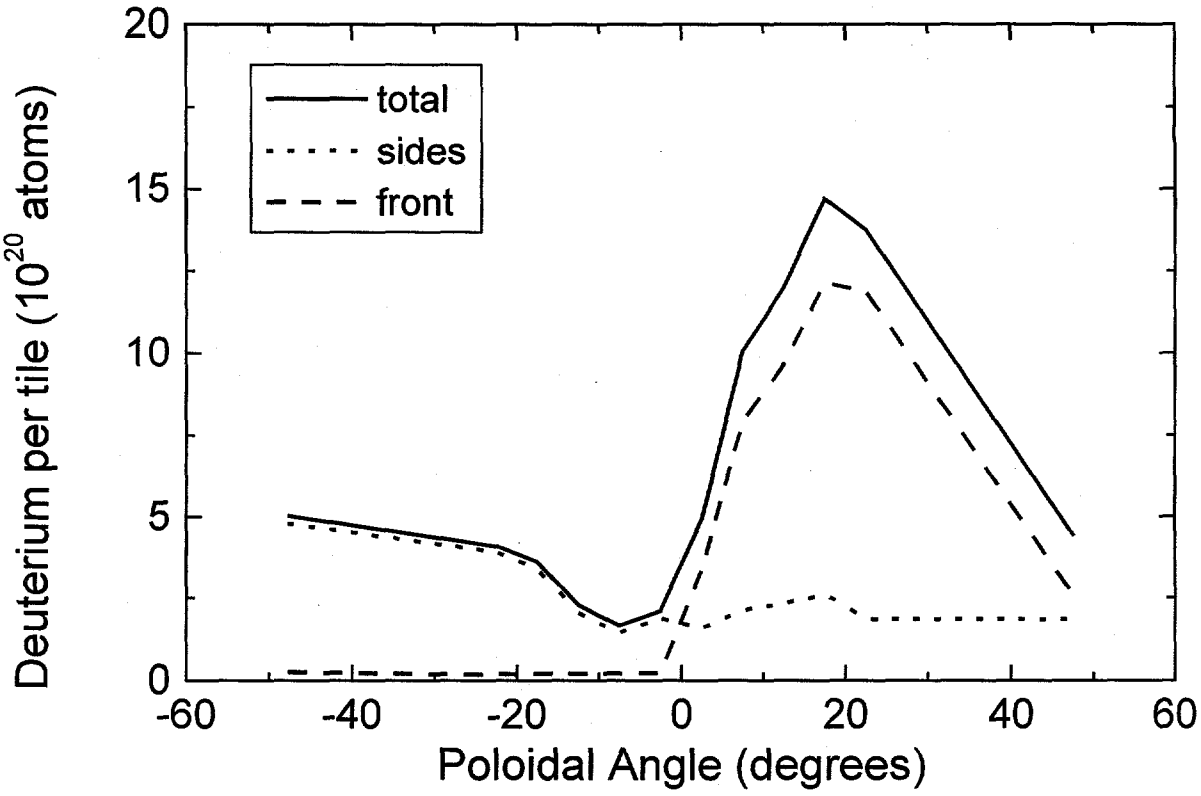

FIG. 5.5.2.1-2 Retained deuterium on tiles from the TFTR bumper limiter.

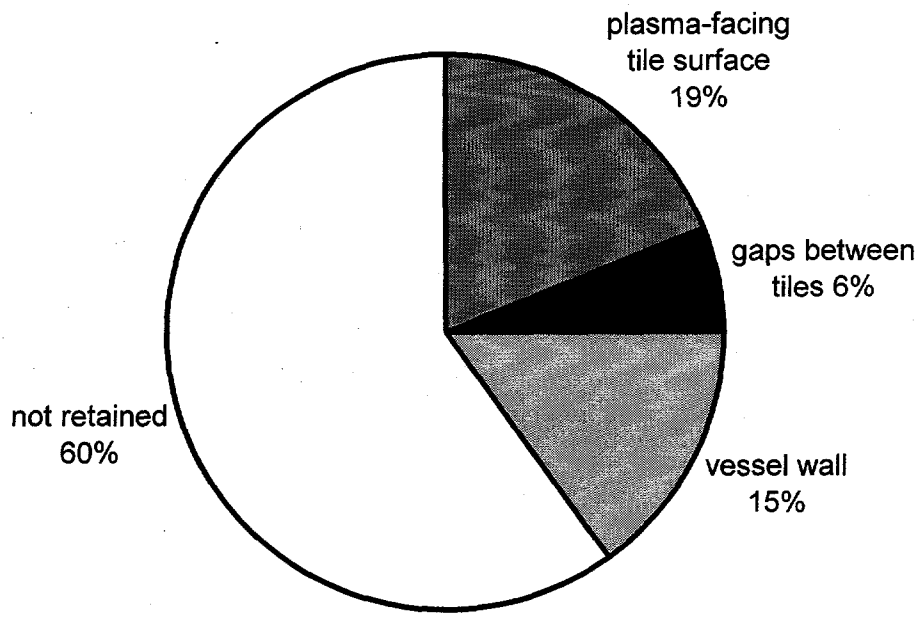

Figure 5.5.2.1-3

Fraction of D fueling retained in various regions of TFTR averaged over period from 1985 to 1991.

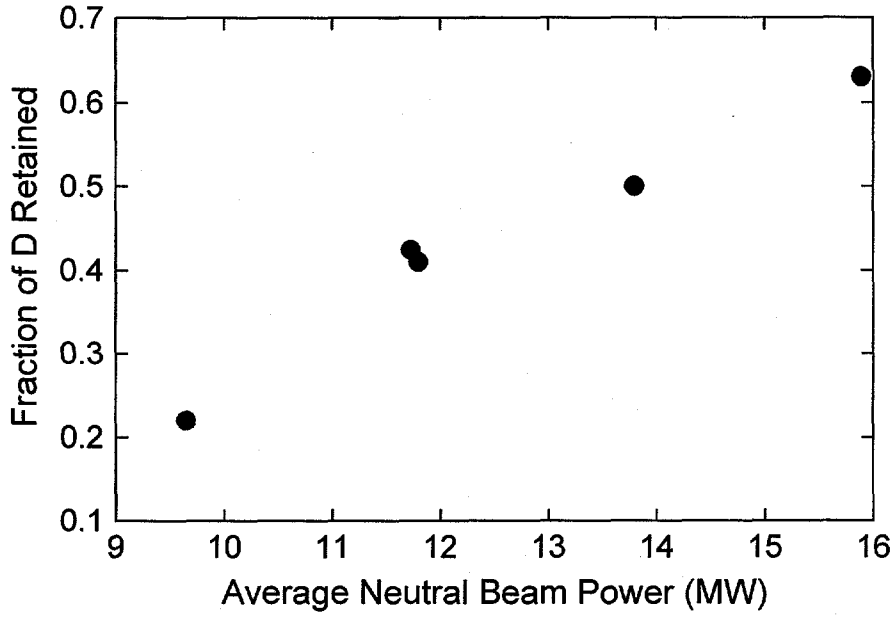

Figure 5.5.2.1-4 Fraction of deuterium retained in TFTR versus average NB power.

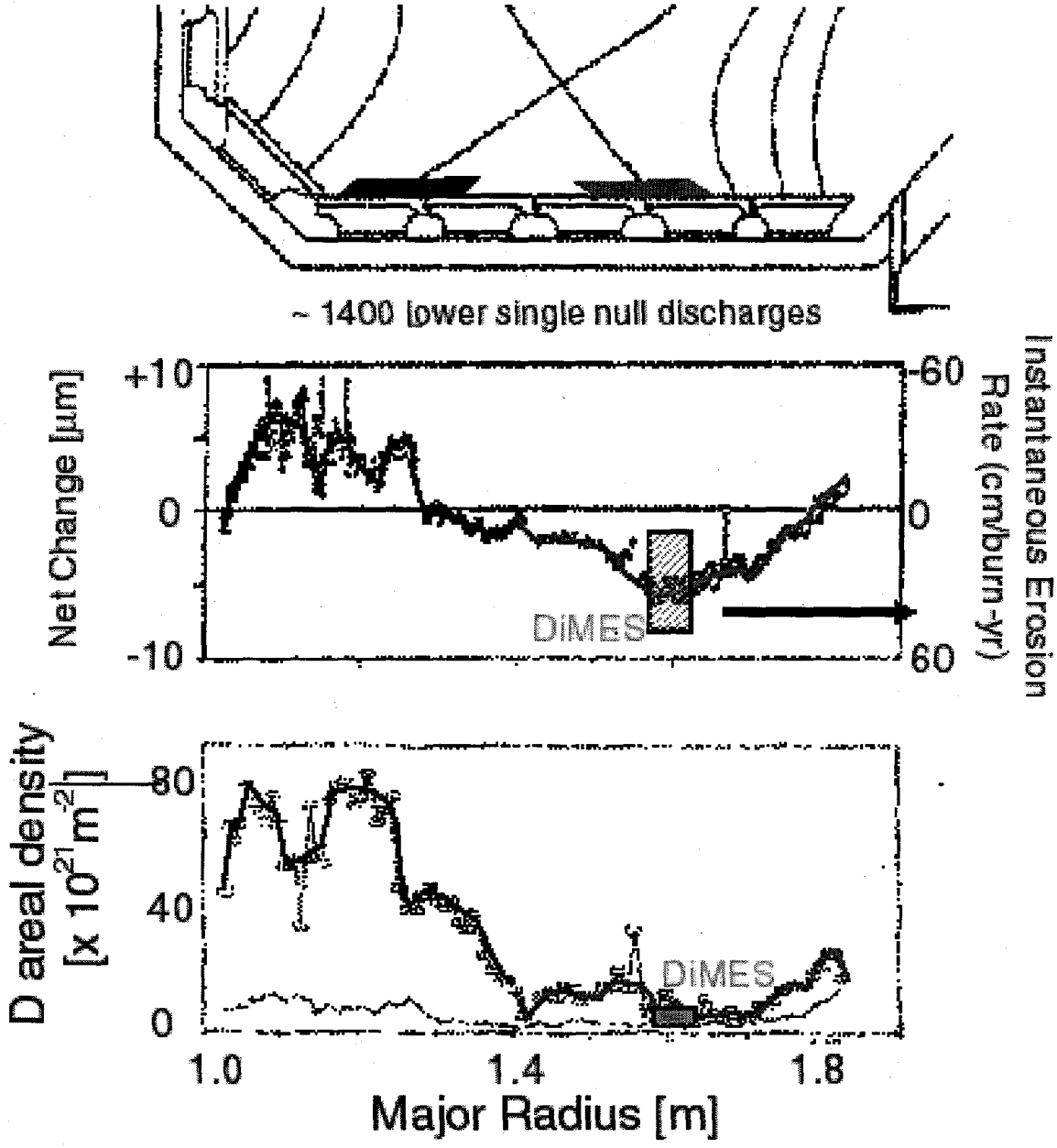

FIG. 5.5.2.1-5 Retained deuterium and net erosion on tiles from the DIII-D divertor.

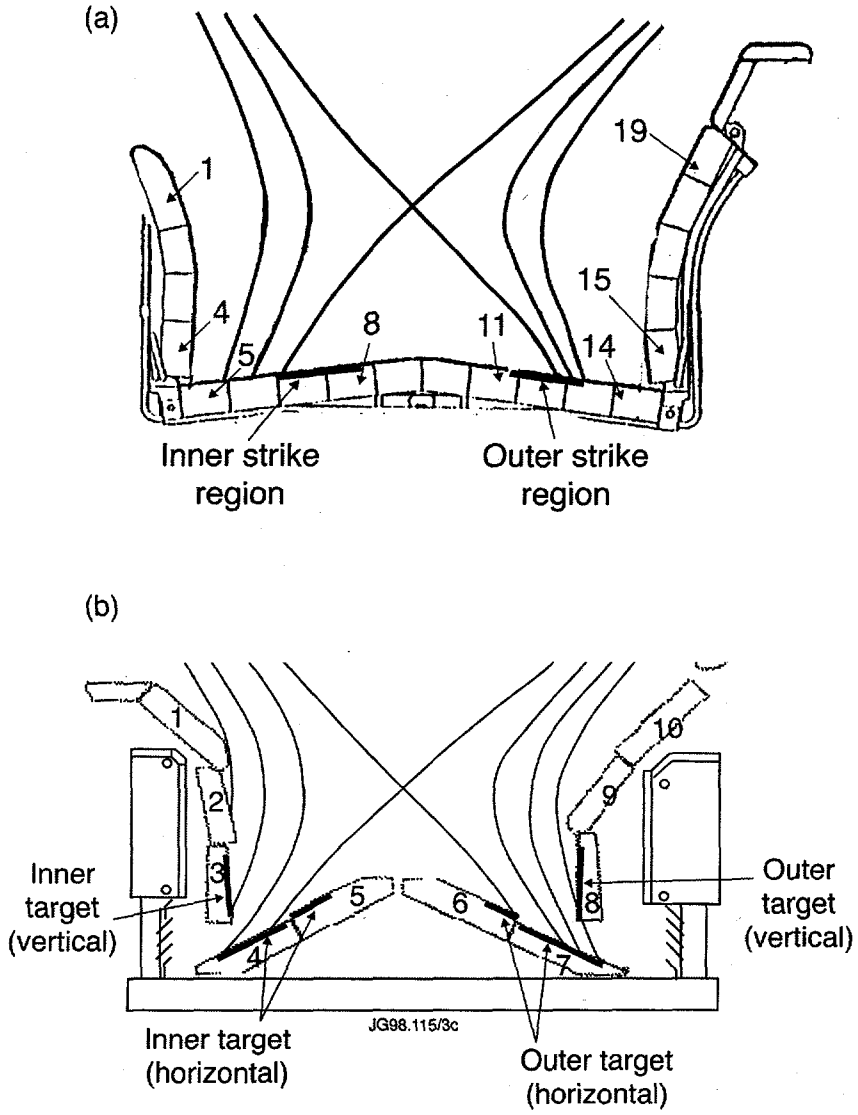

FIG. 5.5.2.1-6 Geometry of JET Mk1 (a) and Mk IIA (b) Divertors

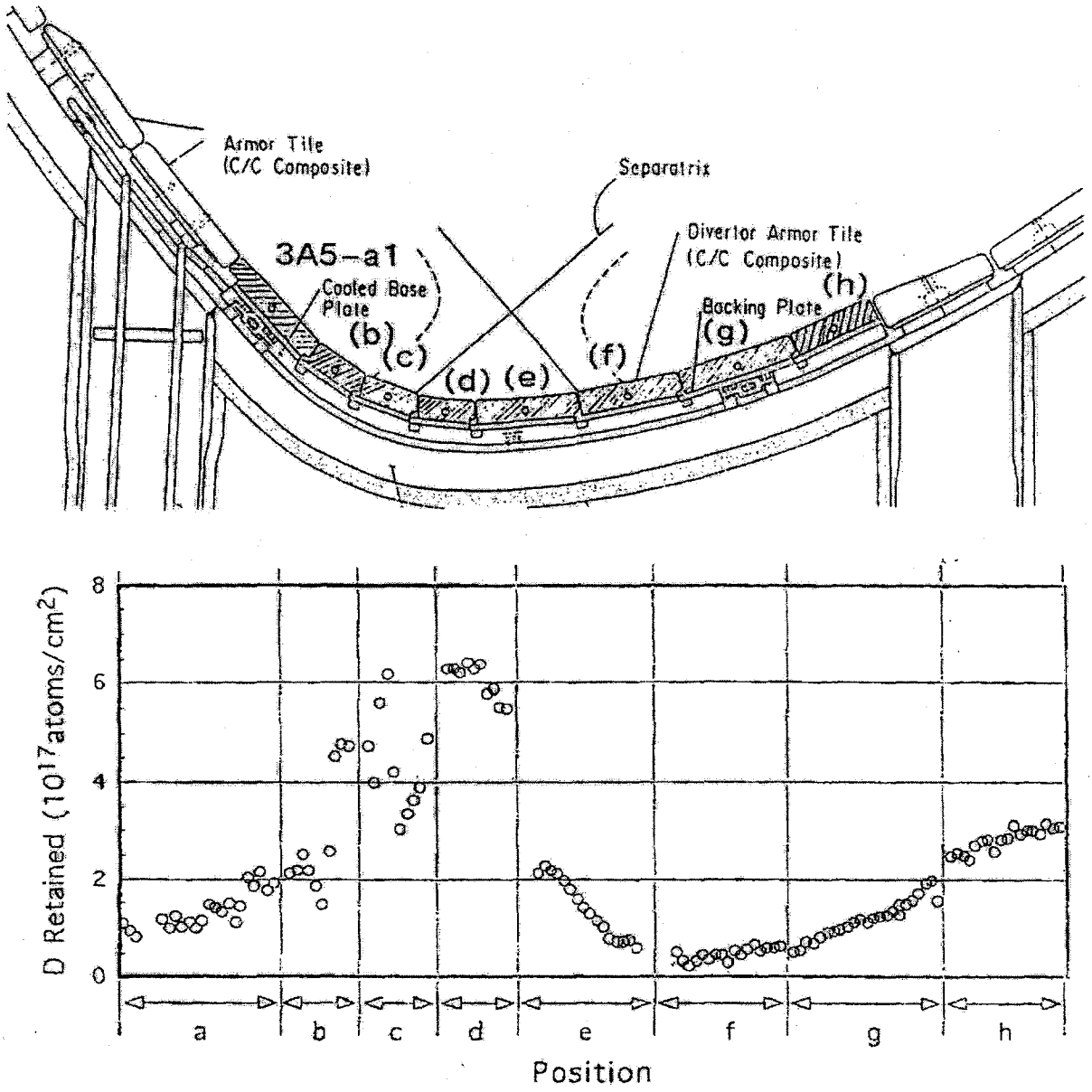

FIG. 5.5.2.1-7 Retained deuterium on divertor tiles in JT-60U.

1 WAMPLER, W. R., DOYLE, B. L., LEE, S. R., PONTAU, A. E., MILLS, B.E., CAUSEY, R.A., BUCHENAUER, D., DYLLA, H.F., ULRICKSON, M.A., and LaMARCHE, P.H., J. Vac. Sci. Technol. **A6** (1988) 2111.

2 DYLLA, H.F. and WILSON, K.L., editors, *Tritium Retention in TFTR*, Princeton Plasma Physics Laboratory report PPPL-2523 and Sandia National Laboratory report SAND88-8212 (April 1988).

3 MILLS, B.E., BUCHENAUER, D.A., PONTAU, A.E. and ULRICKSON, M.A., J. Nucl Mater. **162-164** (1989) 343.

4 McGRATH R.T. and BROOKS, J.N., J. Nucl Mater. **162-164** (1989) 350.

5 PITCHER, C.S., et. al, J. Nucl. Mater. **196-198** (1992).

6 RAMSEY, A.T., BUSH, C. E., DYLLA, H.F., OWENS, D.K., PITCHER, C.S., and ULRICKSON, M.A., Nucl. Fusion **31** (1991) 1811

7 Unpublished proceedings of workshops of the TFTR Deuterium-Tritium Materials Physics Group, Princeton Plasma Physics Laboratory 1987 to 1991.

8 MUELLER, D. et. al., Proceedings of the 17th IEEE/NPSS Symposium on Fusion Engineering, San Diego, CA, October 6-10, 1997.

9 ULRICKSON,M.A., DYLLA, H.F., and LaMARCHE, P.H., J. Vac. Sci Technol. **A6** (1988) 2001.

10 SKINNER , C.H., et. al., J. Nucl. Mater. **241-243** (1997) 214.

11 SKINNER , C.H., et. al., J. Vac. Sci Technol. **A14** (1996) 3267.

12 WALSH, D.S., DOYLE B.L.and JACKSON, G.L., J. Vac. Sci Technol **A10** (1992) 1174.

13 WONG C.P.C., et. al., J. Nucl. Mater. **196-198** (1992) 871.

14 WONG, C.P.C., WHYTE, D.G., BASTASZ, R.J., BROOKS, J.N., WEST, W.P., and WAMPLER, W.R., J. Nucl Mater. **258-263** (1998) 433.

15 WHYTE, D,G., COAD, J.P., FRANZEN, P., MAIER, H, Nucl. Fusion, to appear.

16 WAMPLER, W.R., LABOMBARD, B., LIPSCHULTZ, B., MCCRACKEN, G.M., PAPPAS, D.A., and PITCHER, C.S, J. Nucl Mater. **266-269** (1999) 217.

17 GREENWALD, M. et al, Nuclear Fusion **37** (1997)793.

18 COAD, J.P., et. al., J. Nucl Mater. **162-164** (1989) 533.

19 COAD, J. P., and FARMERY, B, Vacuum **45** (1994) 435.

20 COAD, J. P., J. Nucl. Mater **226** (1995) 156.

21 COAD, J.P., ANDREW, P.L., and PEACOCK, A.T, Physica Scripta (1999) to appear.

22 COAD, J.P., RUBEL, M., and WU, C.H., J Nucl Mater. **241-243** (1997) 408.

23 SARTORI, R., SAIBENE, G., GOODALL, D.H.J., USSELMANN, E., COAD, J.P., and HOLLAND, D., J. Nucl. Mater. **176-177** (1990) 624.

24 ANDREW, P., et.al., J. Nucl. Mater **266-269** (1999) 153.

25 MAYER, M., BEHRISCH, R., ANDREW, P., and PEACOCK, A.T, J. Nucl. Mater. **241-243** (1997) 469.

26 PEACOCK, A.T. et. al., J. Nucl. Mater. **266-269** (1999) 423.

27 FRANZEN, P., et. al., Nuclear Fusion (1999) to appear.

28 HILDEBRANDT, D., AKBI, M., JUTTNER, B., and SCHNEIDER, W., J. Nucl. Mater. **266-269** (1999) 532.

29 SCHLEUSSNER, D., et. al., J. Nucl. Mater. **266-269** (1999) 1296.

30 MAIER, H., KRIEGER, K., BALDEN, M., ROTH, J., and the ASDEX UPGRADE TEAM, J. Nucl. Mater. **266-269** (1999) 1003.

31 MAIER, H., et. al., European Physical Society, Maastrich, June 1999.

32 GAUTHIER, E., GROSMAN, A., VALTER, J., J. Nucl. Mater. **220-222** (1005) 506.

33 GRISOLIA, C., GHENDRIH, PH., PEGOURIE, B., and GROSMAN, A., J. Nucl. Mater. **196-198** (1992) 281.

34 GAUTHIER, E., et. al., Wall conditioning technique development in tore Supra with permanend magnetic field by ICRF wave injection, J. Nucl. Mater. **241-243** (1997) 553.

35 LOARER, T., GROSMAN, A., CHATELIER, M., GHENDRIH, PH., CHAMOUARD, C., MIODUSZEWSKI, P. K., SONATO. P., and UCKAN, T., Active density control with ergodic divertor and pump limiters on Tore Supra, J. Nucl. Mater. **220-222** (1995) 183.

36 AMEMIYA, S., MASUDA, T., ANDO, T., KODAMA, K., and MASAKI, K., J. Nucl. Mater. **220-222** (1995) 443.

37 MASAKI, K., ITER expert group meeting, Naka Japan, October 1998.

38 MASAKI, K., et. al., Tritium retention in graphite inner wall of JT-60U, Fusion Engineering and Design **31** (1996) 181.

39 R. Doerner et. al., J. Nucl Mater. **176** (1989) 954.

40 LIEBERMAN M.A., and LICHTENBERG, A.J., Principles of plasma discharges and materials processing, Wiley, New York (1994).

41 NAKANO, T., TOYODA, H., and SUGAI, H, Jap. J. Appl. Phys. **30** (1992) 2908 and 2912.

42 MOTLAGH, S., and MOORE, J., J. Chem. Phys. **109** (1998) 432.

43 ECKSTEIN, W., GARCIA-ROSALES, C., ROTH, J., and OTTENBERGER, W., Sputtering Data, Report IPP9/82, February 1993, Max-Planck Institute for Plasma Physics, Garching Germany.